



Late Quaternary glacier and sea-ice history of northern Wijdefjorden, Svalbard

LIS ALLAART , JULIANE MÜLLER, ANDERS SCHOMACKER, TOM A. RYDNINGEN, LENA HÅKANSSON, SOFIA E. KJELLMAN , GESINE MOLLENHAUER AND MATTHIAS FORWICK

BOREAS



Allaart, L., Müller, J., Schomacker, A., Rydningen, T. A., Håkansson, L., Kjellman, S. E., Mollenhauer, G. & Forwick, M.: Late Quaternary glacier and sea-ice history of northern Wijdefjorden, Svalbard. *Boreas*. <https://doi.org/10.1111/bor.12435>. ISSN 0300-9483.

The deglaciation history and Holocene environmental evolution of northern Wijdefjorden, Svalbard, are reconstructed using sediment cores and acoustic data (multibeam swath bathymetry and sub-bottom profiler data). Results reveal that the fjord mouth was deglaciated prior to 14.5 ± 0.3 cal. ka BP and deglaciation occurred in a stepwise manner. Biomarker analyses show rapid variations in water temperature and sea ice cover during the deglaciation, and cold conditions during the Younger Dryas, followed by minimum sea ice cover throughout the Early Holocene, until c. 7 cal. ka BP. Most of the glaciers in Wijdefjorden had retreated onto land by c. 7.6 ± 0.2 cal. ka BP. Subsequently, the sea-ice extent increased and remained high throughout the last part of the Holocene. We interpret a high Late Holocene sediment accumulation rate in the northernmost core to reflect increased sediment flux to the site from the outlet of the adjacent lake Femmilsjøen, related to glacier growth in the Femmilsjøen catchment area. Furthermore, increased sea ice cover, lower water temperatures and the re-occurrence of ice-rafted debris indicate increased local glacier activity and overall cooler conditions in Wijdefjorden after c. 0.5 cal. ka BP. We summarize our findings in a conceptual model for the depositional environment in northern Wijdefjorden from the Late Weichselian until present.

Lis Allaart (lis.allaart@uit.no), Anders Schomacker, Tom A. Rydningen, Sofia E. Kjellman and Matthias Forwick, Department of Geosciences, UiT The Arctic University of Norway, Tromsø N-9037, Norway; Juliane Müller and Gesine Mollenhauer, Helmholtz Centre for Polar and Marine Research, Alfred Wegener Institute, Bremerhaven D-27568, Germany; Lena Håkansson, Department of Arctic Geology, The University Centre in Svalbard (UNIS), Longyearbyen N-9171, Norway; received 30th August 2019, accepted 13th February 2020.

Ocean-induced ice melt plays a major role in accelerated mass loss and instability along the margins of glaciers and ice sheets (e.g. Bindschadler 2006; Straneo *et al.* 2010; Straneo & Heimbach 2013; Cook *et al.* 2016). In Svalbard (74–81°N, 10–35°E), submarine melt, collapse and frontal ablation of modern tidewater glaciers have been shown to be controlled primarily by ocean temperature (Luckman *et al.* 2015).

The Svalbard region and neighbouring high-latitude areas are more strongly affected by the current climate warming than lower latitudes, an effect often referred to as the Arctic amplification (Screen & Simmonds 2010; Serreze & Barry 2011). Currently, the extent and thickness of the perennial sea ice cover in the Arctic Ocean north of Svalbard decreases every year, the glaciers in Svalbard experience unprecedented mass loss, and the sea surface and air temperatures of Svalbard are increasing (Adakudlu *et al.* 2019).

Fifty-seven percent of the land area of Svalbard is covered by glaciers (Nuth *et al.* 2013) and more than 60% of glaciers in Svalbard have tidewater margins, all of which are affected by warming sea surface temperatures (Błaszczuk *et al.* 2009). Furthermore, 13–90% of the glaciers have been estimated to be of surge-type (e.g. Hagen *et al.* 1993; Jiskoot *et al.* 1998; Sevestre & Benn 2015; Farnsworth *et al.* 2016). These glaciers have quasi-periodic dynamically driven advances that are not directly related to mass balance (Meier & Post 1969; Sharp 1988; Sevestre & Benn 2015; Aradóttir *et al.* 2019).

In order to understand how the present and projected future global warming will affect the glaciers in Svalbard, and to extend the knowledge of the past climate on Svalbard beyond instrumental records, high-resolution climate records from the Late Pleistocene and Holocene are needed (Hald *et al.* 2004; Renssen *et al.* 2005; Jakobsson *et al.* 2014; McKay & Kaufman 2014). Fjord sediments and submarine geomorphology can provide such information about past glacier and climate fluctuations and, seen in relation to variations in seawater temperatures, allow us to place the current glacier retreat into a broader perspective (e.g. Howe *et al.* 2003; Forwick & Vorren 2009).

The Fram Strait, west of Svalbard, is the main gateway of oceanic and atmospheric heat exchange between the Arctic and the Atlantic Oceans (Aagaard *et al.* 1987; Jakobsson *et al.* 2007; Beszczynska-Möller *et al.* 2011). The distal branch of the North Atlantic Drift, the West Spitsbergen Current, transports warm saline Atlantic Water masses (temperature >3 °C and salinity >34.9 PSU) northward along the west coast of Svalbard, whereas the East Spitsbergen Current carries cold and less saline water-masses from the Arctic Ocean into the Barents Sea and up along the west coast of Spitsbergen as the Spitsbergen Coastal Current (Fig. 1). The intrusion of Atlantic Water from the West Spitsbergen Current is responsible for an increased heat flux to western Svalbard fjord systems where it affects the distribution of surface water-masses, sea ice and, hence, the extents of

ice caps and glaciers (Nilsen *et al.* 2008). Spielhagen *et al.* (2011) inferred that the strongest inflow of Atlantic Water into the Arctic Ocean in the past 2.0 ka has taken place during the last 30 years. The climate of Svalbard is, therefore, highly sensitive to even small changes in the configuration of the surrounding water and air masses, making the archipelago a key location for studying the impact and interaction of oceanic and atmospheric forcing on glaciers and climate (Fig. 1; Aagaard 1982; Aagaard *et al.* 1987; Hanssen-Bauer *et al.* 1990; Rogers *et al.* 2005; Cottier *et al.* 2010; Rasmussen *et al.* 2013; Miller *et al.* 2017).

Spitsbergen is the largest island of the archipelago and the termination of the Late Weichselian and postglacial evolution on northern Spitsbergen remains poorly constrained (Ślubowska *et al.* 2005; Bartels *et al.* 2017). The overall objective of this study is to reconstruct the postglacial environmental evolution of northern Spitsbergen based on the integration of swath bathymetry, high-resolution seismic data and multi-proxy analyses of sediment cores from the outer part of Wijdefjorden (Fig. 1). The specific aims are to (i) reconstruct the deglacial dynamics and the postglacial sedimentary environments; (ii) reconstruct sea-ice extent and water temperatures during the deglaciation and the Holocene; and (iii) identify causal links between glacier retreat, warming sea surface temperatures and sea-ice extent.

Physiographic and geological setting

Wijdefjorden is a ~110-km-long, north–south oriented fjord in northern Spitsbergen (Fig. 1). It is the longest fjord in the archipelago, and it follows the strike of the Billefjorden Fault Zone (Dallmann 2015). The fjord width increases from 3.3 km at its head to 25 km at its mouth. Vestfjorden, a tributary fjord, joins the western side of Wijdefjorden ~30 km north of the fjord head (Fig. 1C). A cross-fjord sill, ~8 km wide (in N–S direction) and with a water depth of ~60 m, is located ~50 km south of the study site (Fig. 1C). It crosses the fjord from Straumtangene to Surtfjellet and divides Wijdefjorden into an outer (northern) and inner (southern) basin (Fig. 1C; Kowalewski *et al.* 1990). Another, narrower sill occurs where Vestfjorden and Austfjorden merge (Fig. 1C). Maximum water depth in the inner basin exceeds 240 m (Hald & Korsun 1997). The sea floor in the outer basin slopes towards the fjord mouth, where it reaches depths >140 m (Fig. 1).

A conductivity-temperature-depth (CTD) profile collected from the study area in July 2017 reveals stratified water-masses composed of three layers, comparable to other Svalbard fjords (Figs 2, 3; cf. Svendsen *et al.* 2002; Nilsen *et al.* 2008; Cottier *et al.* 2010; Forwick *et al.* 2010). In years of enhanced flux of Atlantic Water, a portion of this water-mass can reach the outer part of Wijdefjorden through a branch of the cross-shelf Hinlopen Trough (Nilsen 2007). This exchange is limited to

the area north of the sill at Straumtangene and depths between ~0 and 100 m (for locations see Fig. 1; Nilsen 2007). The intermediate layer in Wijdefjorden is most likely Transformed Atlantic Water, formed by mixing of the surface water and intruding Atlantic Water (Fig. 2; e.g. Svendsen *et al.* 2002). The catchment of the Wijdefjorden system is 4375 km² and the fjord receives runoff from four tidewater glaciers (Mittag-Lefflerbreen, Stubendorffbreen, Midtbreen and Nordbreen) and more than 30 glacier-fed rivers (Fig. 1C; Hagen *et al.* 1993). Mittag-Lefflerbreen and Stubendorffbreen drain the Lomonosovfonna ice cap and Midtbreen and Nordbreen drain the Åsgardfonna ice cap (Fig. 1C). Mittag-Lefflerbreen, Stubendorffbreen and Nordbreen are suggested surge-type glaciers (Farnsworth *et al.* 2016). In northern Wijdefjorden, the large lake Femmilsjøen (7.6×1.3 km) acts as a sediment trap for discharge from the northwestern part of Åsgardfonna and the outlet from the lake supplies the central part of the study area with fresh water (Fig. 1C). A surge-type glacier, Longstaffbreen, terminates in the eastern corner of the lake (Fig. 1C; Hagen *et al.* 1993). In 1993, the total number of glaciers in the catchment area was 202, covering an area of 1831 km². This number is assumed to be smaller today (Nuth *et al.* 2013). Aerial and satellite images reveal that the sediment laden meltwater plumes from these sources are deflected to the south on the western side of the fjord and towards the north on the eastern side (TopoSvalbard © Norwegian Polar Institute 2019). However, in fjords on Svalbard, changing wind directions and tidal changes can cause both large interannual, seasonal and short-term variations in the surface water distribution (e.g. Svendsen *et al.* 2002; Forwick *et al.* 2010; Skarðhamar & Svendsen 2010).

The bedrock of the eastern side of Wijdefjorden is primarily composed of Palaeoproterozoic to Mesoproterozoic metamorphic rocks, whereas the bedrock on the western side contains predominantly Devonian sedimentary rocks (Dallmann 2015). These rocks are separated by the Billefjorden Fault Zone that strikes subparallel to the fjord axis.

Glacial history

Last Glacial Maximum

During the Late Weichselian, Wijdefjorden acted as a pathway for an ice stream that extended to the shelf break north of Spitsbergen, draining the northern sector of the Svalbard-Barents Sea Ice Sheet (Landvik *et al.* 1998; Ottesen *et al.* 2005, 2007; Ottesen & Dowdeswell 2006; Hormes *et al.* 2013). The maximum extent most likely occurred between 25–20 cal. ka BP (Landvik *et al.* 1998; Batchelor *et al.* 2011; Hormes *et al.* 2013; Ingólfsson & Landvik 2013; Hughes *et al.* 2015). Ice thickness has been estimated to be up to 1.5 km in the inner part of Wijdefjorden (Hormes *et al.* 2013).



Fig. 1. Overview map of Svalbard and the study area. A. International Bathymetric Chart of the Arctic Ocean (IBCAO; Jakobsson *et al.* 2012). B. Map of Svalbard with place names mentioned in the text and the locations of the major ocean currents around Svalbard. Location of currents after Hogan *et al.* (2017). C. Detail map of Wijdefjorden, red box marks the study area and dashed white lines denote the location of sills. Background map © Norwegian Polar Institute (2019).

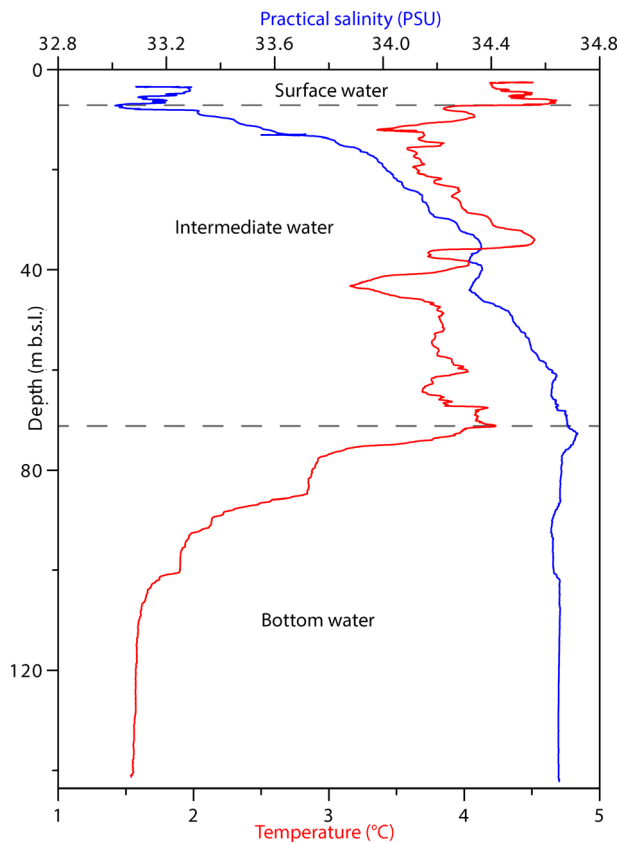


Fig. 2. Water temperature and salinity at a central site in the study area; measurements carried out on 28th July 2017. See Fig. 3 for location.

Deglaciation

In central Spitsbergen, deglaciation initiated at the shelf *c.* 14.1 cal. ka BP and the ice retreated stepwise to the inner fjords until *c.* 11.2 cal. ka BP (Svendsen *et al.* 1992; Elverhoi *et al.* 1995a; Hald *et al.* 2004; Forwick & Vorren 2009; Baeten *et al.* 2010). However, the timing of the onset of deglaciation in northern Spitsbergen remains poorly constrained. Exposure ages from Amsterdamøya and Danskøya, northwestern Svalbard (for location see Fig. 1), suggest onset of glacier-free conditions between 18 and 15 ka ago (Landvik *et al.* 2003). In northern Hinlopen Strait, disintegration of the ice sheet was initiated at 16.7 cal. ka BP; the retreat was rapid and Atlantic Water entered the area *c.* 15 cal. ka BP (Koç *et al.* 2002; Ślubowska *et al.* 2005; Batchelor *et al.* 2011). In outer Woodfjorden, partial break-up started prior to 14.6 ka BP and terrestrial areas were deglaciated before *c.* 10.2±0.26 cal. ka BP (Fig. 1; Bartels *et al.* 2017; Røthe *et al.* 2018). The inner part of Woodfjorden deglaciated around 10.0 cal. ka BP (Hansen 2014; Bartels *et al.* 2017). In Wijdefjorden, exposure ages from Tyrkampen (~450 m a.s.l.) and Dellingsstupa (~150 m a.s.l.) indicate that the fjord-adjacent mountain plateaux were deglaciated by 18.1±1.2 and 14.4±1 ka ago, respectively (Fig. 1C; Hormes *et al.* 2013). Sediment

cores from the fjord (adjacent to Dellingsstupa) reveal that grounded ice had retreated from this part already prior to 11.5 cal. ka BP, indicating a time-lag of *c.* 3 ka between deglaciation on land and in the fjord (Braun 2019). Furthermore, Braun (2019) suggests that the deglaciation of the innermost part of Wijdefjorden was delayed until *c.* 7.2 cal. ka BP.

Hormes *et al.* (2013) proposed that the inner part of Wijdefjorden (Fig. 1B) still contained a lot of grounded glacier-ice during the Younger Dryas (YD). Farnsworth *et al.* (2018) identified a major glacial advance in de Geerbukta (Fig. 1B) that took place during the overall deglaciation phase, indicating that the deglaciation was much more dynamic than previously thought.

Postglacial development

During the Early Holocene, glaciers in Spitsbergen were comparably small (Mangerud & Svendsen 1990, 1992; Svendsen & Mangerud 1997; Forwick & Vorren 2009; Baeten *et al.* 2010; Røthe *et al.* 2015, 2018). However, glaciers most likely persisted throughout the entire Holocene (Hald *et al.* 2004; Forwick & Vorren 2009).

On Svalbard, the orbitally driven Holocene Thermal Optimum occurred time-transgressively and is recognized earlier in marine than terrestrial environments (Salvigsen *et al.* 1992; Hald *et al.* 2004; Blake 2006; Salvigsen & Høgvard 2006; van der Bilt *et al.* 2015). In marine environments, the Holocene Thermal Optimum was dominated by inflow of Atlantic Water, strong seasonality and limited ice-rafting. In the Isfjorden and van Mijenfjorden areas, it occurred between *c.* 11.2–8.2 cal. ka BP (Fig. 1B; Hald *et al.* 2004; Forwick & Vorren 2009; Rasmussen *et al.* 2013). In Wahlenbergfjorden (Fig. 1B) it occurred between *c.* 11.3–7.7 cal. ka BP, and was associated with a reduced summer sea ice cover (Bartels *et al.* 2018).

In northern Svalbard, the hydrographic dominance in Wahlenbergfjorden changed from Atlantic to Arctic Water at *c.* 7.7 cal. ka, resulting in colder conditions (Bartels *et al.* 2018). Meanwhile, the shelf areas were still influenced by warm Atlantic Water (Ślubowska *et al.* 2005; Rasmussen *et al.* 2007, 2013). Another cooling interval, with glacier growth and extended sea ice cover from *c.* 5 cal. ka BP, is recognized both in lacustrine (Svendsen & Mangerud 1997; van der Bilt *et al.* 2015) and marine records (Hald *et al.* 2004; Forwick & Vorren 2009; Baeten *et al.* 2010; Müller *et al.* 2012; Rasmussen *et al.* 2013). In northern Svalbard, the glaciers and sea ice cover in Wahlenbergfjorden expanded between *c.* 3.1–0.2 ka BP, while the bottom waters warmed, probably due to the isolating effect of sea ice (Fig. 1B; Bartels *et al.* 2018). This Middle-to-Late Holocene cooling interval is often termed the Neoglacial (e.g. Landvik *et al.* 2005; Bartels *et al.* 2018; Lovell *et al.* 2018).

The last cold period of the Neoglacial, the Little Ice Age, lasted between *c.* AD 1200–1900 in Svalbard

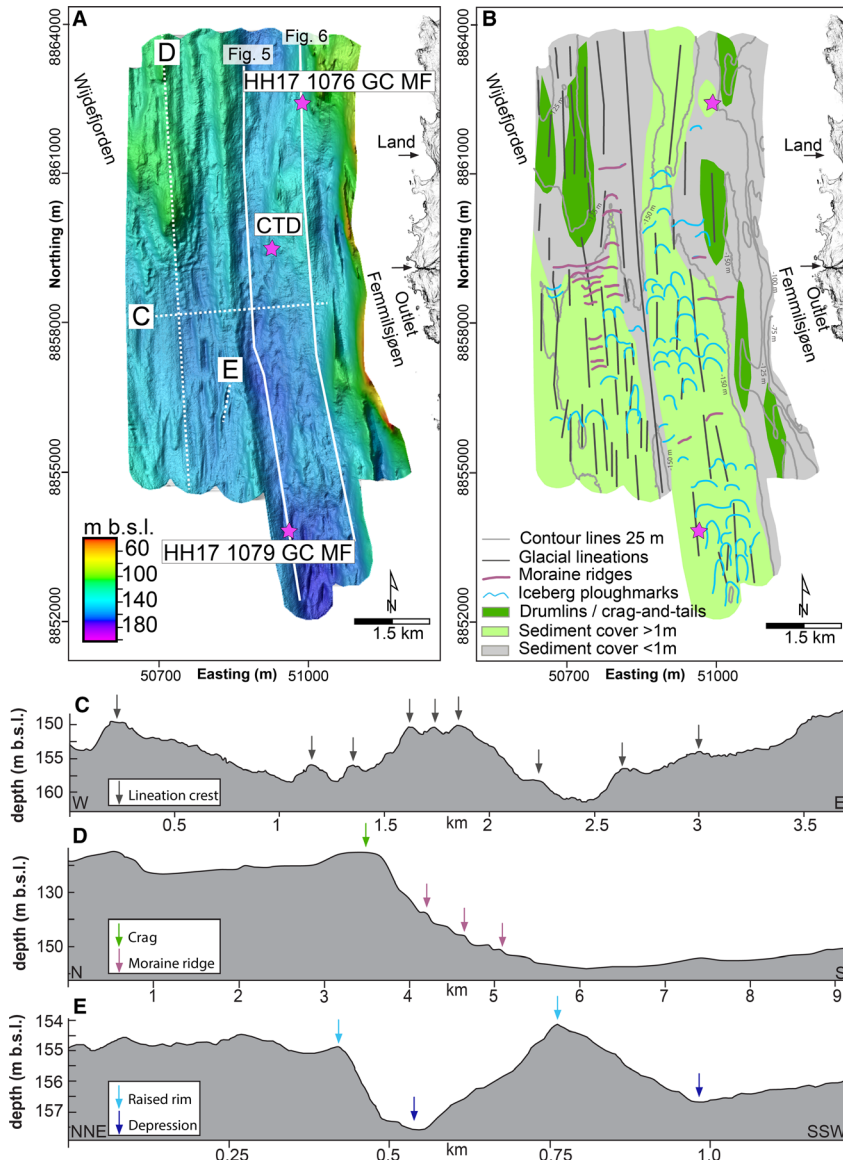


Fig. 3. Sea-floor geomorphology and cross profiles from the study area in northern Wijdefjorden. A. Bathymetry of the study area. Locations of bathymetric profiles across landforms are indicated with white dashed lines (C–E) and location of chirp profiles (Figs 7, 8) are marked with full white lines. Location of cores 1076, 1079 and the CTD station are marked with pink stars. B. Geomorphological map of the sea floor. C–E. Cross profiles of the landforms. In the upper profile, locations of lineation crests are indicated with dark-grey arrows. In the middle profile, location of the crag in one of the crag-and-tails is marked with a green arrow, the pink arrows mark locations of moraine ridges. The lowermost profile shows a cross profile of two iceberg ploughmarks. Light blue arrows mark raised rims, dark blue arrows mark depressions. The coastline (east on the map) is based on a terrestrial DEM from © Norwegian Polar Institute (2019).

(Werner 1993; Salvigsen & Høgvard 2006; van der Bilt *et al.* 2015). It is uncertain whether the early or the later part (Little Ice Age) of the Neoglacial represents the coldest Holocene climatic interval in Svalbard (e.g. Hald *et al.* 2004; Rasmussen *et al.* 2013).

Material and methods

The data providing the basis for this study were collected during a geo-scientific cruise of RV ‘Helmer Hanssen’

owned by UiT (The Arctic University of Norway) from 26th July to 1st August 2017.

Conductivity-temperature-depth (CTD)

The water properties were measured at one central site (latitude 79°48'N, longitude 15°28'E, 149 m depth) in the study area using a Seabird 911 Plus V 5.0 CTD in order to obtain water column sound-velocities for the multibeam survey and for assessing the characteristics of the water-

masses in the study area (Figs 2, 3). Data collection was performed during down- and up-casts at a speed of approximately 1.0 m s^{-1} and an acquisition frequency of 24 Hz.

Bathymetry

Approximately 50 km^2 of swath-bathymetry data were acquired with a hull-mounted 30 kHz Kongsberg Maritime EM 302 multibeam echo sounder (Figs 1, 3). The data set was imported into the Petrel Software in UTM zone 33N (datum: WGS84), and gridded with $5 \times 5 \text{ m}$ horizontal resolution using the convergent interpolation method. The grid was imported into the Global Mapper software, where different vertical exaggerations and illuminations were applied in order to visualize landforms on the seabed. Re-gridding the data set to 10×10 and $20 \times 20 \text{ m}$ grids in Global Mapper (using the same interpolation method) reduced noise in the data set and gave a smoother appearance; hence the $10 \times 10 \text{ m}$ grid was used as the basis for the maps. Submarine landforms were mapped in ESRI ArcMap 10.5 based on their shape and surface expression. Artefacts such as Erik's Horns and 'flappy' outer beams (Jakobsson *et al.* 2016) exist as vague lines in the margins of the data set and where the lines overlap.

Sub-bottom data

Ten high-resolution seismic (chirp) profiles were acquired with a hull-mounted EdgeTech 3300-HM sub-bottom profiler with 4×4 arrays. A frequency range of 2–12 kHz and a 20 ms shot rate of 1 Hz were used. A p-wave velocity of 1600 m s^{-1} was applied to estimate the thickness of the sediment package (Elverhøi *et al.* 1995a; Plassen *et al.* 2004; Forwick & Vorren 2010).

Sediment cores

Two sediment gravity cores, HH17-1076-GC-MF (289 cm, $79^\circ 50' \text{N}$, $15^\circ 30' \text{E}$, 141 m depth; Fig. 4) and HH17-1079-GC-MF (366 cm, $79^\circ 45' \text{N}$, $15^\circ 29' \text{E}$, 163 m depth; Fig. 4), were retrieved using a 6-m-long gravity corer (weight $\sim 1900 \text{ kg}$). The outer and inner diameters of the plastic liners inserted into the steel barrel were 11.0 and 10.2 cm, respectively. The sites were selected based on the detection of sediment packages on the chirp profiles, and in order to get one core north and south of the outlet of Femmilsjøen, respectively. Below, we refer to the cores as core 1076 and core 1079.

Geophysical and geochemical properties

Physical properties, including magnetic susceptibility (loop sensor), fractional porosity and wet bulk density, were measured with a Geotek Multi-Sensor Core Logger (MSCL) at 1-cm steps, prior to core splitting. After

splitting, X-radiographs were acquired using a Geotek Standard X-ray CT System (XCT). Furthermore, line-scan images of the sediment surface were acquired with a Jai L-107CC 3 CCD RGB Line Scan Camera mounted on an Avaatech XRF core scanner.

The Avaatech XRF core scanner was also used to carry out qualitative measurements of the element-geochemical composition of the sediment surfaces using a Rhodium X-ray source. Prior to the measurements, the sediment surface was smoothed and covered with a $4\text{-}\mu\text{m}$ -thick ultralene foil. The measurements were carried out in two runs at 10-mm steps with down-core and cross-core slits of 10 and 12 mm, respectively, using the following settings: (i) 10 kV, $1000 \mu\text{A}$, 10 s counting time, no filter; and (ii) 30 kV, $2000 \mu\text{A}$, 10 s counting time, Pd-thick filter. Data processing was carried out with WinAxil version 4.5.6. The cores were stored at room temperature for 1 day prior to the measurements in order to reduce the influence of water-film formation below the foil due to condensation (Tjallingii *et al.* 2007). The results are presented as element counts normalized to the sum of counts of the 12 most abundant elements (Al, Si, S, K, Ca, Ti, Mn, Fe, Br, Rb, Sr and Zr) to minimize the influence of seawater and matrix effects (e.g. Cuven *et al.* 2011; Davies *et al.* 2015).

Lithostratigraphy

The split-core surfaces were visually described and colour information was obtained using the *Munsell Soil Color Chart*. The distribution of clasts and sedimentary structures were determined from X-radiographs. Clasts $> 2 \text{ mm}$ in diameter were counted at 1-cm intervals on the X-radiographs and considered as ice-rafted debris (IRD; Grobe 1987).

Grain-size analyses

Four grams of wet samples were subsampled at 5-cm intervals for grain-size analyses. The samples were first treated with acetic acid and hydrogen peroxide to remove carbonate and organic matter. The samples were washed with distilled water in order to neutralize pH. They were subsequently dried at 30°C for 24 h and samples of 0.2 g sediment were suspended in demineralized water and put on a shaking table for 24 h. One drop of Calgon solution (water softener) was added to the suspended samples and they were put in an ultrasonic cleaner for 3–8 min to prevent clay particles from flocculating. Subsequently, the samples were analysed three times in a Beckman Coulter LS 13 320 Particle Sizing Analyser for fractions between 0.4 and $2000 \mu\text{m}$. The mean of the three runs was used for grain-size statistics in the GRADISTAT v. 8 Excel-software (Blott & Pye 2001), and the data were plotted as heat maps in MATLAB using the script '3D plot of grain size data in sedimentology v. 1.2.0.0' (Fredin 2020).

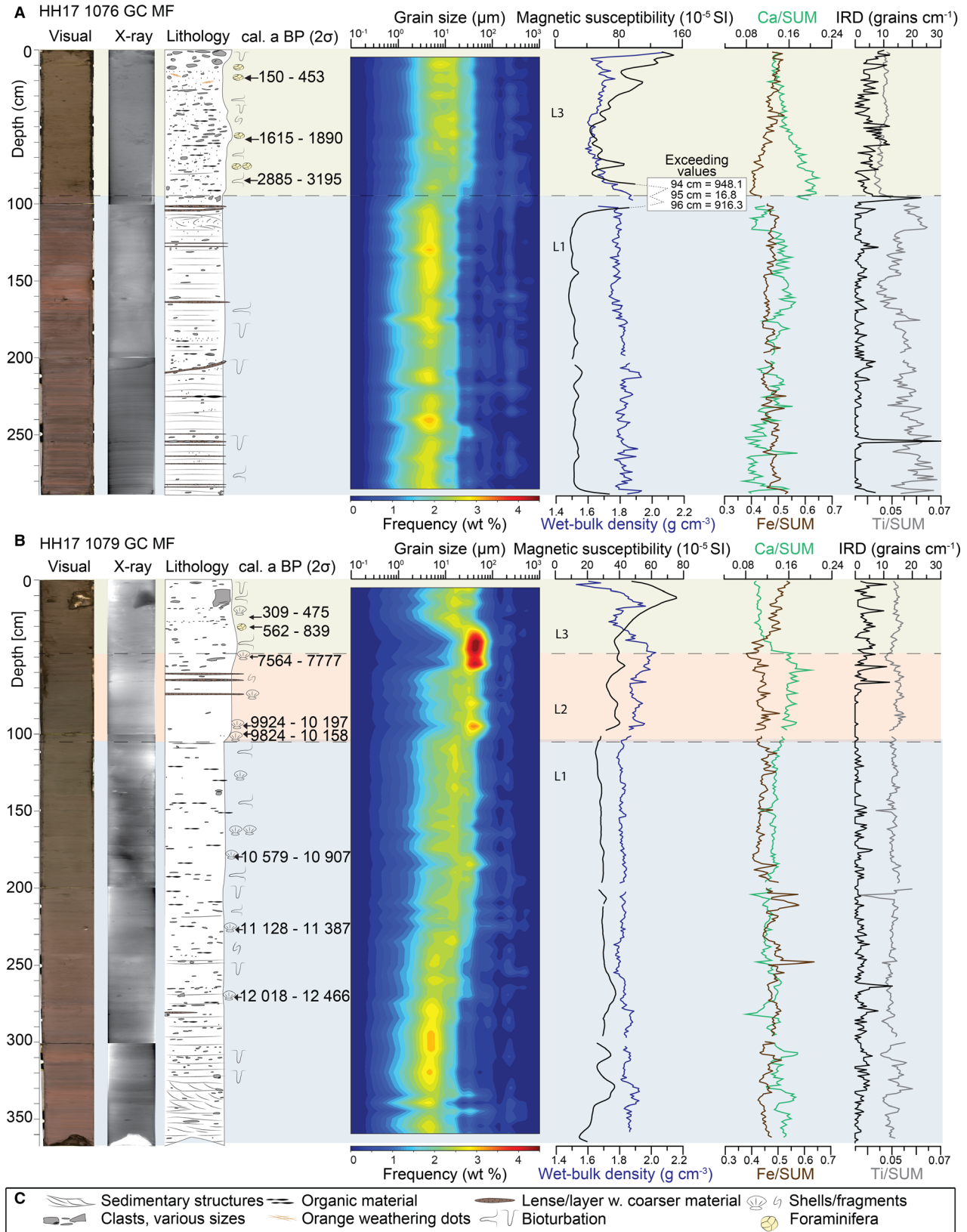


Fig. 4. Composite logs of cores 1076 and 1079. A, B. Core photograph, X-ray image, lithological log, and physical and elemental properties of cores 1076 and 1079. C. Legend for the lithological logs.

Chronology

Seven macrofossils (bivalve shells) from core 1079 were identified on the X-radiographs and sampled for radiocarbon dating. Additionally, four samples of the benthic foraminifera species *Cibicides lobatulus* were picked; three from core 1076 and one from core 1079. The radiocarbon measurements were carried out at the Ångström Laboratory at Uppsala University, Sweden. Age-depth models were constructed for cores 1076 and 1079 with the Bayesian based code BACON (v. 2.3.5) working within the open-source statistical environment R (v. 3.6.0; R Core Team 2017) (Blaauw 2010; Blaauw & Christen 2011). The Marine13 calibration curve with a built-in reservoir age of 440 years was used, applying a local ΔR value of 70 ± 30 years (Mangerud *et al.* 2006; Reimer *et al.* 2013). The reported radiocarbon ages are given in calibrated kilo years before present (cal. ka BP; BP = 1950), according to Reimer *et al.* (2013). Sediment accumulation rates for the dated intervals of cores 1076 and 1079 were extracted from BACON using the `accrate.depth` function. The age and accumulation rate of the undated interval (366–270.5 cm) of the lower part of core 1079 were manually extrapolated based on sediment similarity with the lowermost dated interval (226.5–270.5 cm) and the accumulation rate of this interval.

Organic geochemical analyses

Core 1079 was subsampled ($\sim 10 \text{ cm}^3$ per sample) for bulk organic geochemical and biomarker analyses at the same depths as for the grain-size analyses. Samples were freeze-dried and subsequently homogenized using an agate mortar. For determination of total organic carbon (TOC) contents, $\sim 100 \text{ mg}$ of sediment was weighed into ceramic crucibles, treated with $500 \mu\text{L}$ of 12 N HCl (37%) to remove carbonate and analysed by means of a carbon-sulphur determinator (CS 2000, Eltra). For the analyses of highly branched isoprenoids (HBIs) and glycerol dialkyl glycerol tetraethers (GDGTs), $\sim 9 \text{ g}$ of sediment was ultrasonically extracted using a mixture of dichloromethane and methanol (2:1 v/v; $3 \times 6 \text{ mL}$) with the supernatants being combined and concentrated using rotary evaporation. Prior to the extraction, 7-hexylnonadecane (7-HND) and C_{46} -GDGT were added as internal standards for quantification of HBIs and GDGTs, respectively. Separation of apolar and polar lipid fractions was achieved by open-column silica chromatography using *n*-hexane and dichloromethane:methanol (1:1 v/v) as eluents, respectively. For the identification and quantification of HBIs, apolar fractions were run on a gas chromatograph (Agilent Technologies 7890B; 30 m DB 1MS column; 0.25 mm diameter; 0.25 μm film thickness) coupled to a mass selective detector (Agilent Technologies 5977B; 70 eV; 230 °C ion source temperature). The GC temperature

programme was: 60 °C (for 3 min), 150 °C ($15 \text{ }^\circ\text{C min}^{-1}$), 320 °C ($10 \text{ }^\circ\text{C min}^{-1}$). Identification of HBIs was based on comparison of their retention times and mass spectra with published chromatograms and mass spectra (e.g. Belt 2018). Molecular ions m/z 350 and 346 for IP_{25} and the $\text{C}_{25:3}$ HBI Z-triene were quantified in relation to the fragment ion m/z 266 of 7-HND. These ratios were normalized using instrumental response factors obtained for each compound. The polar fraction was re-dissolved in hexane:isopropanol (99:1 v/v), filtered through a PTFE filter and diluted with hexane:isopropanol (99:1 v/v) before instrumental analysis with high-performance liquid chromatography-mass spectrometry. Calculation of the RI-OH' index using hydroxylated isoprenoid GDGTs (OH-GDGTs) and conversion of these RI-OH' values into seawater temperatures followed Lü *et al.* (2015) and Park *et al.* (2019). IP_{25} is applied as a sea-ice proxy, while the related $\text{C}_{25:3}$ HBI Z-triene (HBI-III) is interpreted to reflect pelagic conditions permitting phytoplankton productivity (Belt 2018). Both data sets are normalized to TOC.

Sea-floor geomorphology: description and interpretation

The water depths in the study area range from 60 to 175 m (Fig. 3). The eastern fjord side has a maximum gradient of 6°. We describe and interpret the identified glacial landforms based on their appearance and surface expression. Postglacial sediments drape the landforms, but the seabed still mimics the shape of all landforms, i.e. the measurements of the heights, widths and lengths relate to their (modern) appearance in the multibeam data.

Drumlins, crag-and-tails, and glacial lineations

Six elongated ridges with drop shape (tapering distal ends) oriented subparallel to parallel to the fjord axis occur in the northwestern and eastern part of the data set (Fig. 3). These ridges are 1500–4000 m long, 15–40 m high and 140–660 m wide. The southern, proximal sides of the landforms are generally smooth. Based on the orientation (sub)parallel to the fjord axis and the asymmetric morphology, we interpret these landforms as drumlins, and crag-and-tails, formed by streaming grounded ice (e.g. Stokes & Clark 2002; Ottesen & Dowdeswell 2009; Benn & Evans 2010; Dowdeswell *et al.* 2010; Fransner *et al.* 2016; Allaart *et al.* 2018). Similar landforms occur in Rijpfjorden ($\sim 140 \text{ km NE}$ of Wijdefjorden) and Lomfjorden (Fig. 1; Fransner *et al.* 2017; Streuff *et al.* 2017).

Sixty-seven elongated ridges and appurtenant grooves are oriented subparallel to the fjord axis. They overprint the drumlins and crag-and-tails (Fig. 3). The ridges are 400–2800 m long, 100–200 m wide and their length-to-width ratios exceed 10:1. One very long ridge ($>9 \text{ km}$) occurs in the central part of the study area. The vertical

amplitudes of single ridge-groove pairs are 1–2 m. Due to the subparallel orientation to the fjord axis, the length-to-width ratio (>10:1) and their ridge-groove morphology, we interpret these landforms as glacial lineations formed by streaming, grounded ice (Clark 1993; King *et al.* 2009). The long lineation is interpreted as a mega-scale glacial lineation, in agreement with Ottesen *et al.* (2005) who identified mega-scale glacial lineations at the mouth of Wijdefjorden.

Moraine ridges

Nineteen fjord-transverse, slightly undulating ridges have been identified (Fig. 3). They are 185–1080 m long, 17–300 m wide and 0.8–3 m high. Where the ridges occur in groups, the distances between the crests are ~130 m. Their cross profiles are symmetric and they overprint the glacial lineations. Due to their transverse orientation and symmetric cross profiles, these ridges are interpreted as moraine ridges formed during stillstands and/or re-advances of the grounding line, similar to observations from other Spitsbergen fjords (e.g. Ottesen & Dowdeswell 2006; Baeten *et al.* 2010; Kempf *et al.* 2013; Flink *et al.* 2015; Streuff *et al.* 2017).

Iceberg ploughmarks

Fifty-nine N–S oriented, elongated depressions, partly bordered by raised rims parallel to their margins and cross-cutting their northern terminations, occur on the sea floor (Fig. 3). The depressions are typically 170–1120 m long, 100–300 m wide and 1–3 m deep. The surrounding rims are up to 1 m high (arcuate to horse-shoe-shaped rim ridges are mapped; Fig. 3). The depressions are offset by 2–3° with respect to the orientation of the glacial lineations. The landforms overprint all previously described landforms. The assemblage of depression and elevation suggests that erosive and depositional processes acted synchronously. The lower length-to-width ratios, as well as much more irregular shapes compared to the glacial lineations indicate a different genesis. We suggest that these landforms are iceberg ploughmarks formed by grounded icebergs eroding into the shallow sub-sea floor and depositing the material as rims along their paths towards the fjord mouth (Vorren *et al.* 1983; Woodworth-Lynas *et al.* 1991; Lewis *et al.* 2016; Vadakkepuliambatta *et al.* 2016). Ridges cross-cutting the terminations of iceberg ploughmarks are referred to as iceberg plough ridges (Jakobsson & Anderson 2016).

Litho- and seismostratigraphy

Lithostratigraphy – description

Based on lithology, colour, grain size, as well as physical and chemical properties, three lithostratigraphical units

(L1–L3) are defined (Fig. 4). L1 (289–95 cm in core 1076 and 366–105 cm in core 1079) consists of stratified fine silt and clay (strata thickness 0.5–5 cm) with few isolated clasts and colours alternating between red-grey (7.5R 4/2), dark-red (2.5YR 3/3) and red (2.5YR 4/6; Fig. 4). The basal contacts between strata are sharp or gradational. Towards the top of the unit, the stratification becomes less pronounced. Thin black bands (<0.5 cm thick) and thin strata (0.5 cm) of coarser material with sharp lower boundaries occur occasionally. The Fe/SUM and Ca/SUM ratios anti-correlate. The Ti/SUM ratio correlates in core 1079 to Ca/SUM, whereas in core 1076 it anti-correlates (Fig. 4).

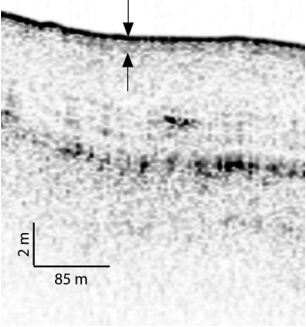
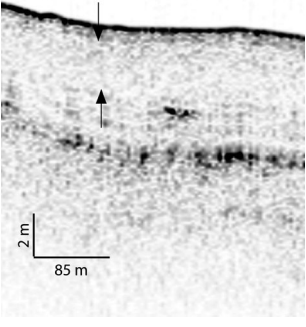
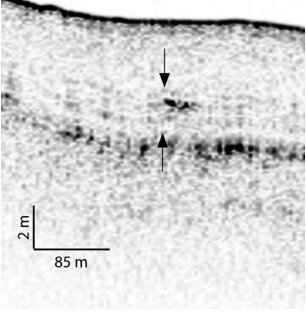
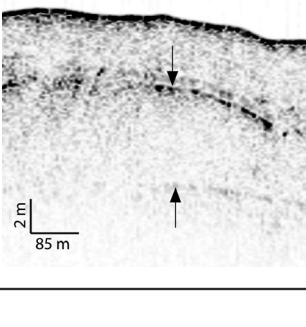
L2 (exclusively between 105–48 cm in core 1079) consists of light greenish grey (7.5YR 4/2) massive clayey silt with abundant, well-preserved bivalve shells (Fig. 4). The basal contact is gradational and defined by the termination of bioturbation and decrease in the number of clasts, compared to L1. Sandy layers (0.5–1 cm thick) with erosional basal contacts occur between 75–60 cm. Clasts are absent between the base of the unit and 60 cm. The Fe/SUM, Ca/SUM and Ti/SUM ratios all correlate in L2 (Fig. 4).

L3 (95–0 cm in core 1076 and 48–0 cm in core 1079) is composed of massive olive-green (2.5Y 4/2) silty clay with a high clast content (Fig. 4). The basal contact is sharp in core 1076 and gradational in core 1079. Abrupt changes in all element-to-sum ratios occur at the transition to L3: the Fe/SUM and Ca/SUM ratios increase and decrease towards the top of L3, respectively. Furthermore, the Ti/SUM ratio decreases. The elemental change is more pronounced in core 1076 compared to 1079 (Fig. 4).

Seismostratigraphy – description

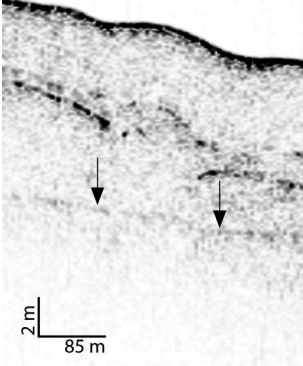
Based on the acoustic attributes and relationship of the intervals to the underlying topography, we establish five acoustic facies (AF1–AF5; Table 1, Figs 5, 6; Elverhøi *et al.* 1983; Syvitski & Praeg 1989; Forwick & Vorren 2010). AF1 and AF2 (Table 1, Figs 5, 6) occur at depths greater than the lengths of the recovered sediments. AF1 is the lowermost facies in the acoustic stratigraphy (Figs 5, 6). It is bounded by a discontinuous top reflection with high reflection amplitude. The acoustic penetration of this facies is little to absent, and it is only detected in the western part of the survey. In central parts of the study area AF1 sub-crops southwards, i.e. the overlying deposits thin out (Fig. 5). AF2 is acoustically transparent and bounded by an upper smooth to hummocky reflection. AF3 varies from acoustically transparent/semi-transparent to stratified. The upper boundary of the unit is discontinuous. AF3 overlies AF1 where AF2 is absent. AF4 is acoustically transparent and drapes the underlying facies and the lower and upper bounding reflections are diffuse. AF5 is semi-transparent.

Table 1. Description and interpretation of acoustic facies from the chirp data from northern Wijdefjorden.

Acoustic facies	Example	Description	Interpretation
AF5		Semi-transparent with a strong upper reflection (representing the sea floor), diffuse lower bounding reflection, 2–4 subparallel internal reflections. The reflections are semi-continuous, drape the underlying units and occur over the entire area but are thinner across obstacles. Thickness <1 m.	The stronger reflections are presumably caused by higher contents of IRD, transparent intervals are interpreted as less clast-rich mud (Forwick & Vorren 2010).
AF4		Acoustically transparent facies, draping the underlying deposits. It disappears/pinches out where the basal reflection of AF1 has very high amplitude in the northern end of the area (bedrock highs). Diffuse upper and lower bounding reflections. Thickness between 1–3.3 m.	Fine-grained, massive mud deposited in a distal glaciomarine environment (Forwick & Vorren 2010; Kempf <i>et al.</i> 2013).
AF3		Usually covers AF2. Acoustically transparent to stratified with subparallel, discontinuous reflections. In the eastern part of the survey area, the facies occasionally rests directly upon AF1. The upper bounding reflection is diffuse and the lower bounding reflection is strong. The thickness varies between 1.6–4 m.	Stratified, glacier-proximal deposits (Forwick & Vorren 2010; Kempf <i>et al.</i> 2013).
AF2		Acoustically transparent facies with varying thickness. Bounded by an upper smooth to hummocky reflection with varying amplitude. Occurs in small hummocks resting on AF1 in the western part of the data set, and as a continuous package with no lower bounding surfaces in the eastern part. In the central part of the surveyed area it appears as a continuous package with an occasional lower bounding surface. Facies thickness varies between 0.8–9.5 m, generally thinning out towards the north.	The transparent character and limited penetration indicate poor sorting/diamictic composition. The facies is acoustically similar to glaciogenic deposits in other Spitsbergen fjords (Elverhøi <i>et al.</i> 1983; Ottesen <i>et al.</i> 2005; Forwick & Vorren 2010; Kempf <i>et al.</i> 2013; Flink <i>et al.</i> 2017). AF2 constitutes the glacial lineations, drumlins and moraine ridges.

(continued)

Table 1. Table tbl1. (continued)

Acoustic facies	Example	Description	Interpretation
AF1		Discontinuous top reflection, conform smooth line where visible, little to no penetration of acoustic signal into this facies. Detected in the central part of the survey area (Fig. 5).	Acoustic basement. The strong upper reflection is interpreted as the surface of the bedrock (Forwick & Vorren 2010).

Litho- and seismostratigraphical interpretation and correlation

AF1 is interpreted to represent bedrock (Elverhøi *et al.* 1983; Forwick & Vorren 2010; Kempf *et al.* 2013) and is clearly distinguished where the acoustic signal has been able to penetrate AF2 (Fig. 5). AF2 is interpreted as compacted glacial deposits and constitutes the glacial lineations, drumlins and moraine ridges mapped in the bathymetry (Figs 3, 5, 6; Elverhøi *et al.* 1983; Ottesen *et al.* 2005; Forwick & Vorren 2010). In the eastern part of the study area (Fig. 6), AF1 (bedrock) and AF2 (compacted glacial deposits) are difficult to distinguish, either because AF2 is too thick for the seismic pulse to penetrate the unit, or AF2 is too thin, i.e. below the vertical resolution of the signal.

AF3 (stratified sediments; Table 1, Figs 5, 6) correlates with L1 (stratified clayey silt; Fig. 4). It is present where depressions in the underlying topography have served as depocentres. AF3/L1 is interpreted as sediments deposited in a glacier-proximal setting in an early phase of the deglaciation (Figs 5, 6; Forwick & Vorren 2009, 2010; Kempf *et al.* 2013). We consider suspension settling from glacial meltwater plumes and river runoff as the main process of deposition; clasts are interpreted as IRD deposited from icebergs or sea ice (e.g. Hald *et al.* 2004; Forwick & Vorren 2009). The stratification may reflect seasonal variation in meltwater and sediment input causing variations in grain size and colour (Svendsen *et al.* 1992; Ó Cofaigh & Dowdeswell 2001; Forwick & Vorren 2009; Streuff *et al.* 2017). The less pronounced stratification towards the top of the unit may indicate a transition to more distal conditions. Glacier-proximal deposits have also been described from other fjords in Spitsbergen (Elverhøi *et al.* 1980, 1983, 1995b; Forwick & Vorren 2009; Baeten *et al.* 2010; Kempf *et al.* 2013).

AF4 (Table 1, Figs 5, 6) correlates with L2 (massive clayey silt, with no/little IRD; Fig. 4). AF4 is only

detected in the central southern part of the study area, similar to L2 that exclusively occurs in core 1079 (Table 1, Figs 4–6). The massive and uniform lithological composition of L2 reflects a stable sedimentary environment. Furthermore, the low IRD content in the lower part is suggested to reflect limited ice rafting in a relatively warm climate. We infer that AF4/L2 represents glaciomarine sediments deposited in a glacier-distal setting (Table 1, Figs 4–6) similar to deposits in other Spitsbergen fjords (e.g. Forwick & Vorren 2009).

AF5 (Figs 5, 6) correlates with L3 (massive clayey silt with IRD; Fig. 4). The acoustically semi-transparent character of AF5 is interpreted to reflect a higher IRD content (Figs 5, 6; Forwick & Vorren 2010). Based on the lithological (massive lithology, abundant clasts and bioturbation) and acoustic characteristics, we infer that AF5/L3 represents glaciomarine sediments deposited in a distal setting (Table 1, Figs 4–6). Suspension settling from meltwater with repeated and increasing supply of IRD derived from icebergs and/or sea ice dominated during deposition of this unit (e.g. Forwick & Vorren 2009).

Chronology and sediment accumulation rates

Description

In core 1076, datable material was exclusively found in the uppermost 90 cm (Fig. 7, Table 2). Thus, the age-depth model is limited to this interval, corresponding to almost the entire L3. The age-depth model suggests that core site 1076 has experienced steady sedimentation during the past $c. 3.1 \pm 0.2$ cal. ka, with sediment accumulation rates varying between 0.04 – 0.08 cm a^{-1} .

The age-depth model for sediment core 1079 indicates that the oldest recovered sediments were deposited prior to 12.4 ± 0.3 cal. ka (Fig. 7). Linear extrapolation from the lowermost dated interval of L1 to the undated interval 366–270.5 cm provides an age-estimate of

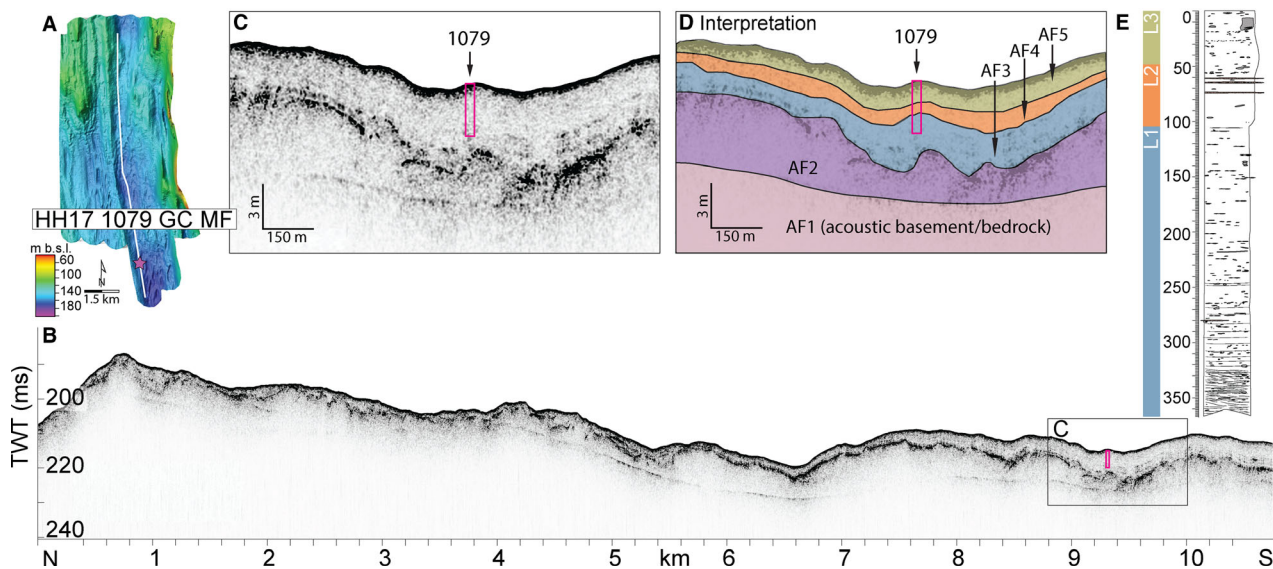


Fig. 5. Sub-bottom profile from the central part of the study area showing the glacial and postglacial sediment succession in northern Wijdefjorden. A. Bathymetry map with location of the chirp profile (white line) and core 1079 (purple star) indicated. B. The chirp profile with location and approximate penetration depth of core 1079 (pink box). Depth in two-way travel time (TWT). AF1 (bedrock) is seen as a continuous smooth reflection in the lower part of the profile. C. Zoom in on the chirp profile at core location 1079. D. Interpretation of the acoustic facies (see also Table 1). E. Compilation of lithological log of core 1079, lithological units (L1–L3) match corresponding acoustic facies.

c. 14.5 ± 0.3 cal. ka BP for the base of the core (Fig. 7). L1 was deposited from 14.5 ± 0.3 to 9.9 ± 0.3 cal. ka BP and sediment accumulation rates varied between 0.051 – 0.231 cm a^{-1} . L2 was deposited from 9.9 ± 0.3 to 7.1 ± 1.0 cal. ka BP and sediment accumulation rates varied between 0.035 – 0.215 cm a^{-1} . The deposition of L3 took place from 7.1 ± 1.0 cal. ka BP until present with

sediment accumulation rates ranging between 0.005 – 0.125 cm a^{-1} .

Interpretation

The low sediment accumulation rate of 0.005 cm a^{-1} between 5.2 ± 2.5 and 0.5 ± 0.1 cal. ka BP in L3 in core

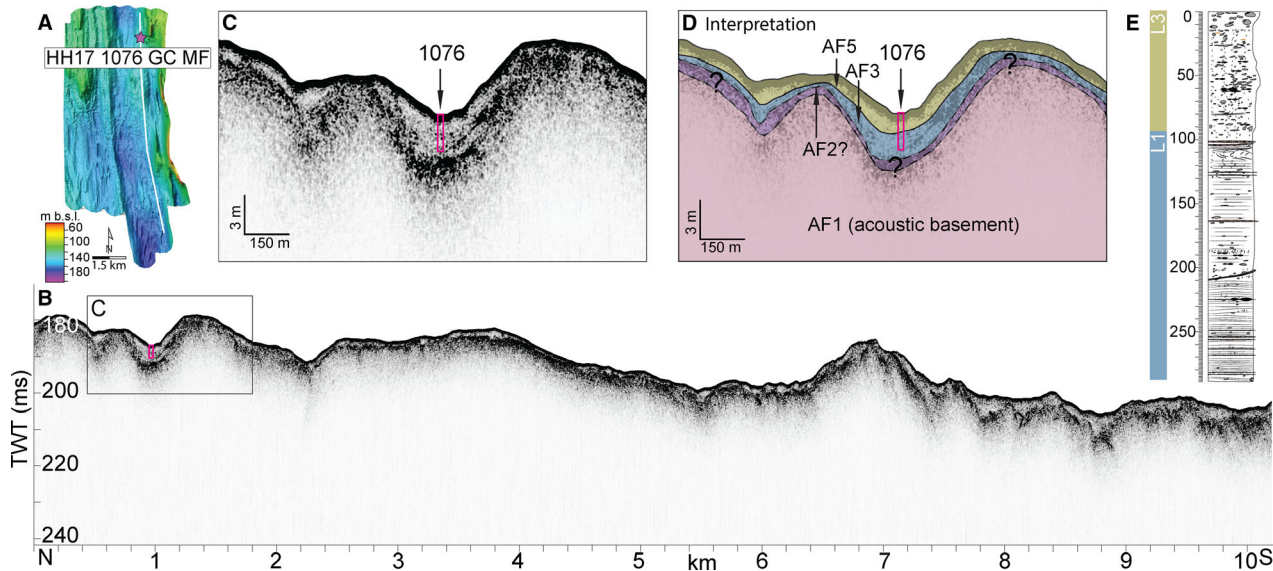


Fig. 6. Sub-bottom profile from the eastern part of the study area showing the glacial and postglacial sediment succession in northern Wijdefjorden. A. Bathymetry map with location of the chirp profile (white line) and core 1076 (purple star) indicated. B. The chirp profile with location and approximate penetration of core 1076 (pink box). Depth in TWT. The sediment thickness is thinner in this profile, compared to the chirp profile for the central part of the study area (Fig. 5). C. Zoom in on the chirp profile at core location 1076. D. Interpretation of the acoustic facies (see also Table 1). It is difficult to distinguish between AF1 and AF2, hence, the extension of AF2 is marked with question marks. E. Compilation of lithological log of core 1076.

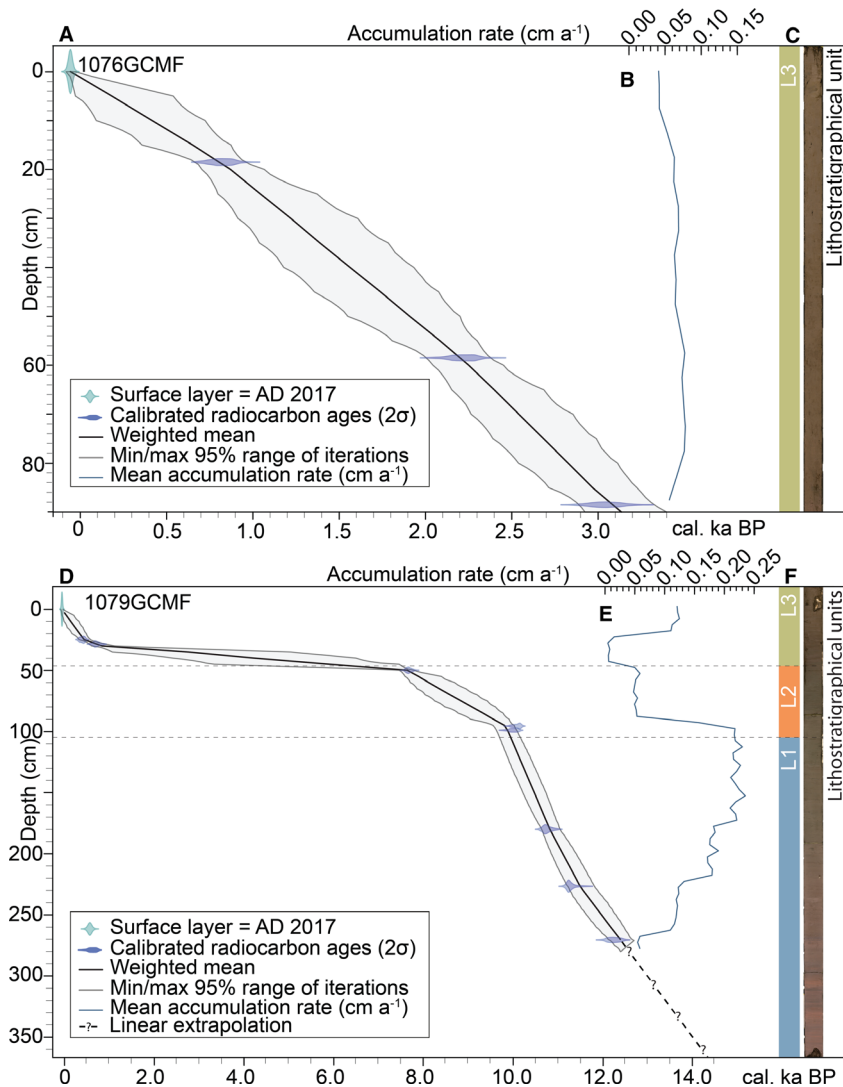


Fig. 7. Age-depth models of cores 1076 and 1079. The ages of the core tops are set to AD 2017. A, D. The age-depth relationship in core 1076 was established for the upper ~90 cm, based on three radiocarbon ages. The model of core 1079 was based on eight radiocarbon ages and manually extrapolated for the lowermost interval (between 366–270.5 cm), i.e. beyond the depth of the lowermost radiocarbon age. Extrapolation was based on the preceding accumulation rate. B, E. Sediment accumulation rates for the dated intervals in cm a^{-1} extracted from BACON. C, F. Core images and corresponding lithostratigraphical units for the cores. See Fig. 4 and Table 2 for details about the radiocarbon ages.

1079 could reflect either a hiatus or temporal sediment starvation at the site. The high age uncertainty (cf. at 5.2 ± 2.5 cal. ka BP, Fig. 7D) and a marked change in the element-to-sum ratios of Ca/SUM and Fe/SUM (Fig. 4B) at the onset of L3 in core 1079 could indicate a hiatus. However, the one order-of-magnitude larger sediment accumulation rate in L3 in core 1076 ($0.04\text{--}0.08 \text{ cm a}^{-1}$) after 3.1 ± 0.2 cal. ka BP contradicts a regional hiatus. Furthermore, the absence of a basal erosional contact and of disturbed sediments in L3 in core 1079 supports the interpretation of the succession to represent period of sediment starvation at the core site of 1079 between *c.* 5 to 0.5 cal. ka BP. A similar low Middle–Late Holocene sediment accumulation rate of 0.006 cm a^{-1} is observed in Wahlenbergfjorden (Fig. 1;

Flink *et al.* 2017), and sediment accumulation rates were generally low in Svalbard in the Middle–Late Holocene (Hald *et al.* 2004; Forwick & Vorren 2009). We attribute the one order-of-magnitude higher Late Holocene sediment accumulation rate observed in 1076 to reflect high sediment flux to the site of 1076 from Lake Femmilsjøen.

Organic geochemical proxies in core 1079

Description

The TOC content varies and fluctuates between 0.50–1.16% (Fig. 8). The highest TOC contents are observed in L1 at 320 cm and in L3 at 35 cm, whereas the lowest TOC content occurs in L1 at 330 cm. The IP_{25} concen-

Table 2. Radiocarbon ages.

Lab. ID	Core	Depth (cm)	Dated material	$\delta^{13}\text{C}$ (‰ VPDB)	^{14}C age (a BP)	Calibrated age range (2σ ; cal. a BP)
Ua-61454	HH17-1079	25	<i>Macoma calcarea</i>	–	832±34	309–475
Ua-62260	HH17-1079	28.5	<i>Cibicides lobatulus</i>	–	1212±60	562–839
Ua-61455	HH17-1079	50	Bivalve shell, indet.	–	7267±44	7564–7777
Ua-58907	HH17-1079	95.5	<i>Macoma calcarea</i>	0.1	9336±35	9924–10 197
Ua-58908	HH17-1079	99	<i>Macoma calcarea</i>	0.3	9267±39	9824–10 158
Ua-58909	HH17-1079	180	<i>Macoma calcarea</i>	0.1	9875±37	10 579–10 907
Ua-58910	HH17-1079	226.5	<i>Bathyrca glacialis</i>	1.8	10 325±36	11 128–11 387
Ua-58911	HH17-1079	270.5	<i>Nuculana pernula</i>	1.4	10 839±41	12 018–12 466
Ua-62259	HH17-1076	18.5	<i>Cibicides lobatulus</i>	–	739±42	150–453
Ua-62261	HH17-1076	58.5	<i>Cibicides lobatulus</i>	–	2241±45	1615–1890
Ua-61196	HH17-1076	88.5	<i>Cibicides lobatulus</i>	–	3300±44	2885–3195

trations range between $0.16\text{--}1.16 \mu\text{g g}^{-1}$ TOC (Fig. 8). The lowest IP_{25} concentrations occur in L1 between 360–350 cm ($0.16\text{--}0.18 \mu\text{g g}^{-1}$ TOC) and in L2 between 65–55 cm ($0.30\text{--}0.35 \mu\text{g g}^{-1}$ TOC). Similar to the TOC content, the IP_{25} concentrations fluctuate more in L1 compared to L2 and L3. The HBI-III concentrations range between $0.04\text{--}9.33 \mu\text{g g}^{-1}$ TOC (Fig. 8). Minimum and maximum concentrations occur in L1 at 275 and 215 cm, respectively. Between 225–180 cm, the concentrations are remarkably high, compared to the rest of the record. The OH-GDGT based seawater temperature estimates range between -2.59 and $+1.16 \text{ }^\circ\text{C}$ (Fig. 8). Minimum temperature occurs in L1 at 310 cm and maximum occurs in L2 at 65 cm.

Interpretation of biomarker records

Fluctuations in the IP_{25} concentrations (Figs 8, 9) indicate repeated changes in sea-ice extent in northern Wijdefjorden during the deposition of the lower part of L1 in core 1079 (360–240 cm; 14.5 ± 0.3 to 11.8 ± 0.3 cal. ka BP). Furthermore, relatively cool seawater temperatures and low HBI-III concentrations depict generally cold conditions during deposition of this interval. The overall decrease in IP_{25} concentrations between 240–110 cm (11.8 ± 0.3 to 10.0 ± 0.3 cal. ka BP) and increasing HBI-III concentrations between 225–215 cm (11.5 ± 0.3 to 11.3 ± 0.3 cal. ka BP) may indicate a decrease in sea ice cover or proximity to the sea-ice edge, both promoting phytoplankton productivity (Belt 2018). Subsequently, the increasing seawater temperatures between 195–105 cm (11.0 ± 0.3 to 9.9 ± 0.2 cal. ka BP) and decreasing HBI-III concentrations between 180–165 cm (10.8 ± 0.2 to 10.6 ± 0.2 cal. ka BP) associated with the continued diminution in IP_{25} concentrations until 105 cm (9.9 ± 0.2 cal. ka BP) are inferred to reflect declining sea-ice extent and reduced ice edge phytoplankton productivity. In L2, where IP_{25} and HBI-III concentrations continue to decrease while seawater temperature increases and reaches a maximum of $+1.16 \text{ }^\circ\text{C}$ (followed by a significant drop to $-1.26 \text{ }^\circ\text{C}$ in the top of the unit), we infer overall increasingly warm conditions and that

the interval reflects the sea-ice minimum for Wijdefjorden during the Holocene.

L3 is characterized by a continuous increase in IP_{25} concentrations. The increase is accompanied by decreasing seawater temperatures and HBI-III concentrations and we infer renewed cold conditions and increasing sea ice.

Compared to alkenone-based sea surface temperature reconstructions for a sediment core from Woodfjorden (Bartels *et al.* 2017) and the CTD profile (Fig. 2), we note that the mainly sub-zero OH-GDGT temperature estimates derived for core 1079 are distinctly low. To what

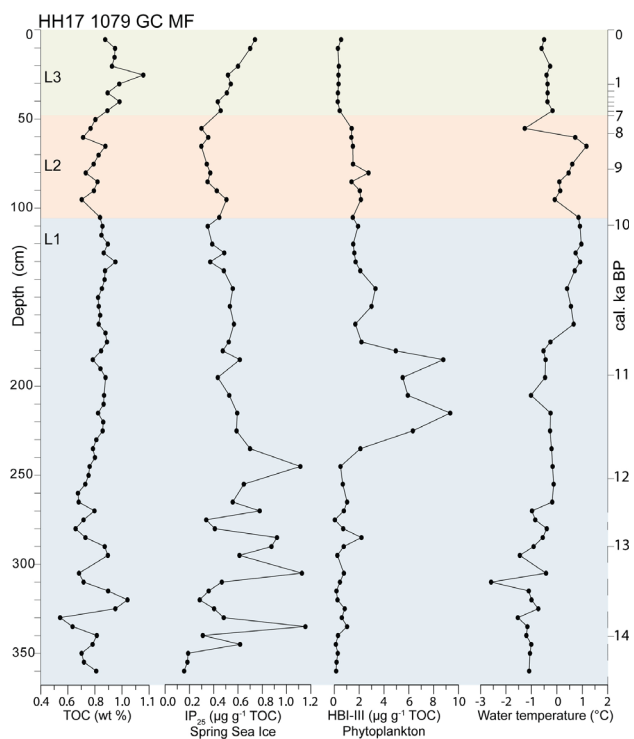


Fig. 8. Biomarker data (TOC, IP_{25} , HBI-III and reconstructed water temperatures) from core 1079 plotted against depth (left side) and age (right side, median ages in cal. ka BP extracted from BACON). Dashed line in the lower part of the age-axis indicates the linearly extrapolated age-interval in the lowermost part of the core.

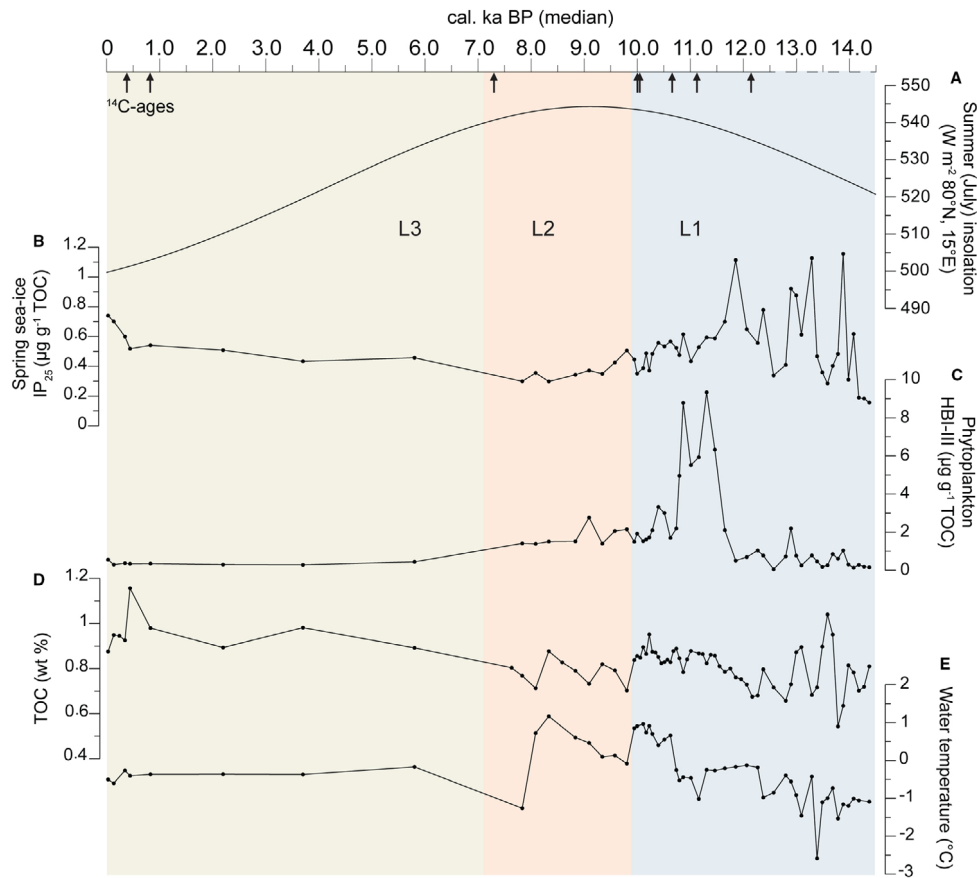


Fig. 9. Biomarkers from core 1079 plotted against median ages (cal. ka BP) extracted from BACON. Dashed line in the right side of the age-axis indicates the linearly extrapolated age-interval in the lowermost part of the core. Lithostratigraphical units L1–L3 are indicated by colours. A. Northern Hemisphere July (21 June–20 July) solar insolation in W m^{-2} at 80°N , 15°E (Laskar *et al.* 2004). B–E. Biomarkers from core 1079.

extent the GDGT data reflect surface or subsurface temperature requires further investigations into the habitat depth of OH-GDGT source organisms and calibration attempts (for detailed discussion see Lü *et al.* 2015; Fietz *et al.* 2016; Park *et al.* 2019). However, the short-term variability and overall trends in temperature seem to be in general agreement with the IP_{25} record.

Environmental evolution of northern Wijdefjorden

Late Weichselian – full glacial conditions

The presence of glacial lineations, drumlins and crag-and-tails, as well as compacted glaciogenic deposits (AF2) indicates that grounded and fast-flowing ice has overridden the area (Figs 3–6, Table 1). Based on the good preservation of the landforms and the presence of postglacial infill of sediment we infer that the landforms were formed during the Late Weichselian (Fig. 10A). This is in agreement with previous reconstructions showing that Wijdefjorden acted as a pathway for an ice stream draining the northwestern part of the Sval-

bard-Barents Sea Ice Sheet during the Late Weichselian (Landvik *et al.* 1998; Ottesen *et al.* 2005; Batchelor *et al.* 2011; Ingólfsson & Landvik 2013).

Late Weichselian – deglaciation

Multiple recessional moraine ridges reflect repeated halts and/or re-advances of the grounded ice during the deglaciation of Wijdefjorden (Figs 3, 10B). These deglaciation dynamics are comparable to other fjords on Svalbard (e.g. Ottesen *et al.* 2008; Baeten *et al.* 2010; Forwick & Vorren 2010; Forwick *et al.* 2010; Kempf *et al.* 2013). The extrapolated basal age for core 1079 (Fig. 7) suggests that the outer part of Wijdefjorden was deglaciated prior to $c. 14.5 \pm 0.3$ cal. ka BP, and the age is in line with the successive younger deglaciation ages in-fjord (Braun 2019). Our deglaciation age from the outer fjord does not conflict with the time-lag further in-fjord between the mountain plateaux and the fjord (Hormes *et al.* 2013; Braun 2019) and the age is comparable to the mouth of Isfjorden, central Spitsbergen, which was deglaciated around 14.1 cal. ka BP (Fig. 1; Mangerud *et al.* 1992). The iceberg ploughmarks were most likely

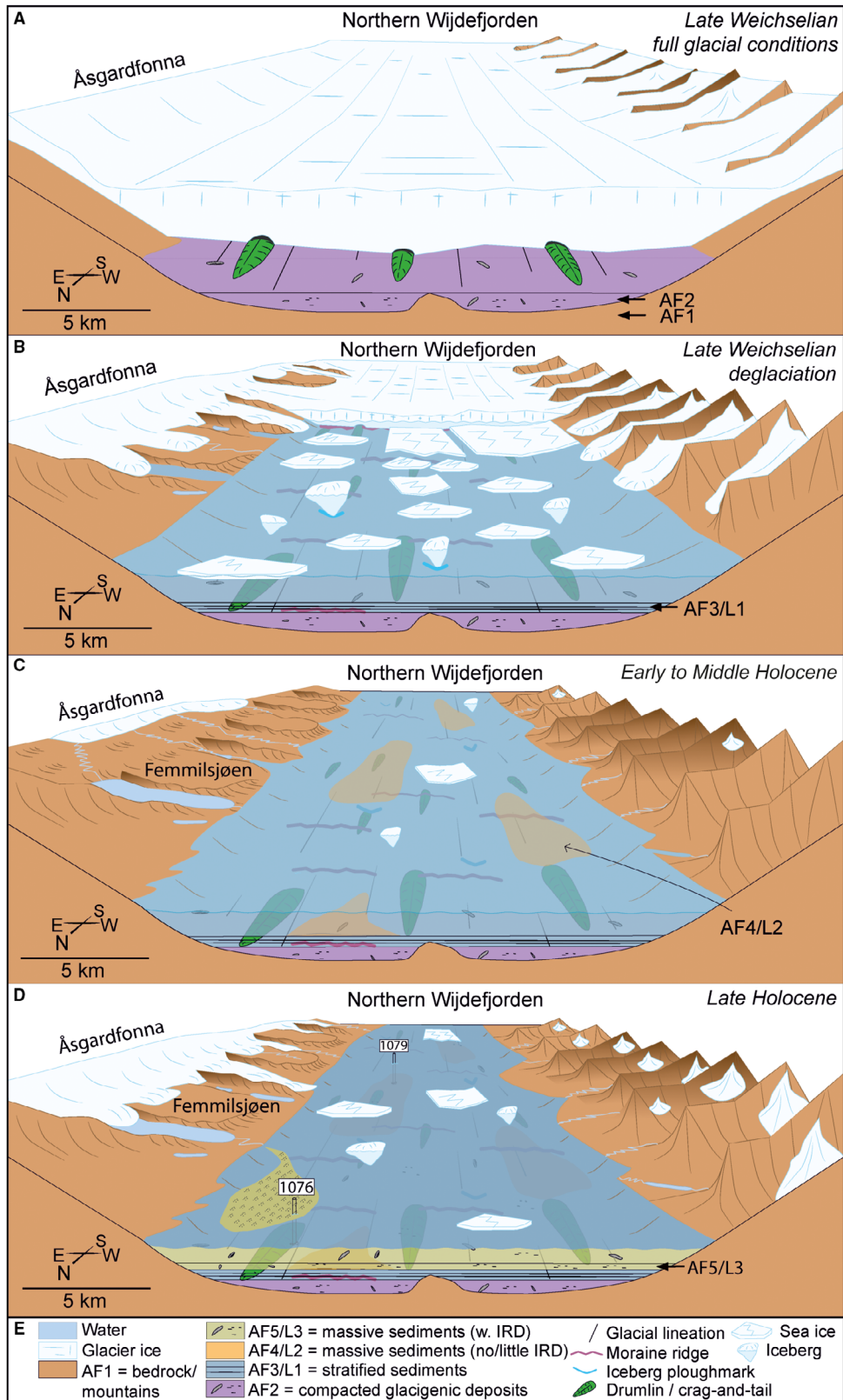


Fig. 10. Conceptual model of the depositional environment in northern Wijdefjorden from the Late Weichselian until present. A. Late Weichselian – full glacial conditions. B. Late Weichselian – deglaciation (the sea ice cover in the graphic is reduced in order to visualize deposition of moraine ridges on the sea floor) C. Early to Middle Holocene. D. Late Holocene, core locations are indicated.

formed by icebergs calving off the retreating glacier front, concurrent with deposition of L1. The weaker stratification towards the top of L1 indicates an increasingly distal glacier setting (Figs 4–6).

Generally, high IP_{25} concentrations and low contents of HBI-III, as well as minimum water temperatures in the lower part of L1 (360–240 cm), point to overall cool conditions and extensive sea ice until $c. 11.7 \pm 0.3$ cal. ka BP. According to the extrapolated age of the core bottom, the time interval $c. 14.5 \pm 0.3$ to 11.7 ± 0.3 cal. ka BP represents the coldest interval in our study. Concurrent IP_{25} maxima and temperature minima are observed at the western continental margin of Svalbard (Müller & Stein 2014; Werner *et al.* 2016). The later part of the interval (12.9–11.7 cal. ka) corresponds to the YD; however, neither a distinct increased cooling nor glacial re-advances spanning the YD are recognized in our data set.

Early to Middle Holocene

From core 1079 where L2 is present, we infer that the Early to Middle Holocene depositional environment in outer Wijdefjorden (Fig. 10C) was characterized by abruptly declining sediment supply and decreasing sea ice cover with synchronous maxima in seawater temperature from $c. 10.6 \pm 0.3$ to 8.1 ± 0.3 cal. ka BP (Fig. 9; 150–60 cm). The absence of unit L2 in core 1076 and the presence in core 1079 indicate that sediment accumulation was limited to bathymetric lows during this period (Figs 3–6, 10). The seawater temperature maxima may indicate increased inflow of warm Atlantic Water leading to limited sea-ice production. Concurrently, enhanced inflow of Atlantic Water was observed in van Mijenfjorden and Isfjorden (Fig. 1B; Hald *et al.* 2004; Forwick & Vorren 2009; Rasmussen *et al.* 2013; Farnsworth *et al.* 2017) and a peak warming in the waters around Svalbard between 10.2–9.2 cal. ka BP is suggested (Mangerud & Svendsen 2018). Furthermore, based on the occurrence of thermophilous molluscs, Early Holocene inflow of warm Atlantic Water is suggested as a potential driver for glacier retreat in St. Jonsfjorden (Farnsworth *et al.* 2017).

The near absence of IRD in the lower part of L2 might be related to the retreat of the main glacier in Wijdefjorden to a position south of the shallow (northern) sill, which limited iceberg and thus IRD flux to the core site (Fig. 1C; e.g. Syvitski *et al.* 1996). We interpret the decreasing sedimentation rate in L2 to reflect increasing glacier-distal conditions (e.g. Andrews & Syvitski 1994; Andrews *et al.* 1994). According to Braun (2019), retreat to this position happened prior to 11.5 cal. ka BP.

In Wijdefjorden the few modern tidewater glaciers are located tens of kilometres (up to 100 km) away from the study area (Fig. 1C). The very low sediment accumulation rate after 7.1 ± 1.0 cal. ka BP could indicate a Holocene glacier minimum in the Wijdefjorden area (Figs 7, 10C), where glaciers had retreated onto land and innermost fjord positions. Similar low sediment accu-

mulation rates are observed in Woodfjorden and Wahlenbergfjorden for the same time interval, where they are attributed to possible but not clearly identified hiatuses (Bartels *et al.* 2017, 2018; Flink *et al.* 2017). Furthermore, it is suggested that most of the glaciers in Woodfjorden around the same time retreated to innermost fjord positions (Bartels *et al.* 2017). We hence find it likely that the overall low sediment accumulation rates in northern Spitsbergen in the Middle Holocene do not represent hiatuses but simply reflect low sediment input from glaciers. The conditions in northern Spitsbergen are thus comparable to central western Spitsbergen during the Early to Middle Holocene, where some of the smaller ice caps disappeared and tidewater glaciers retreated to positions several kilometres farther back than their modern margins (Mangerud & Svendsen 1990; Svendsen & Mangerud 1997; Hald *et al.* 2004; Forwick & Vorren 2009; Baeten *et al.* 2010).

Late Holocene

The Late Holocene was characterized by different sediment fluxes to the core sites 1076 and 1079. This is because core site 1076 is located north of the outlet of Lake Femmilsjøen (Fig. 10D). Glacier growth in the Femmilsjøen catchment area would likely cause higher sediment flux into the lake and, hence, more sediment escaping to Wijdefjorden towards core site 1076 (Fig. 10D). From the biomarkers in core 1079 (Fig. 9), we infer a gradual increase in sea ice cover associated with seawater temperatures around -0.5 °C in northern Wijdefjorden during the Late Holocene. Abundant IRD in L3 in both cores (Fig. 4) indicates increased ice-rafting and most likely Late Holocene glacier re-advances in Wijdefjorden. Similar conditions prevailed in Wahlenbergfjorden where IP_{25} concentrations increased from $c. 3.1$ cal. ka BP (Bartels *et al.* 2018) and in Woodfjorden where the seawater temperatures were equally low; however, the sea-ice extent was suggested to be reduced (Bartels *et al.* 2017). Neoglacial glacier re-advances are suggested in both Woodfjorden and Wahlenbergfjorden (Bartels *et al.* 2017, 2018; Flink *et al.* 2017).

The sediment accumulation rates increased markedly after $c. 0.5$ cal. ka BP at site 1079 (Figs 4, 5, 7D, 10D, Table 2). The almost synchronous increase in IP_{25} concentrations after $c. 0.7 \pm 0.2$ cal. ka BP, with a maximum in the modern sediments, indicates more sea ice towards the Late Holocene, comparable to conditions in the Hinlopen Strait (Jernas *et al.* 2013). We interpret the IRD signal in the upper part of L3 (increase from ~ 25 cm in core 1076 and the IRD peaks from ~ 35 cm in core 1079) and the increased sediment accumulation rate in core 1079 as a signal of further increased glacial activity in all of the Wijdefjorden area from $c. 0.5$ cal. ka BP. At the same time, the sea-ice extent increased. Together, this is interpreted to represent the onset of the Little Ice Age in the area.

Conclusions

- Streamlined landforms (glacial lineations, drumlins, and crag-and-tails) and the presence of compacted glacial deposits (seismic unit AF2) indicate that northern Wijdefjorden was covered by a grounded ice stream during the Late Weichselian.
- The outer part of Wijdefjorden was probably deglaciated prior to *c.* 14.5±0.3 cal. ka BP.
- The deglaciation occurred stepwise leading to the deposition of recessional moraines during halts and/or minor re-advances. Iceberg ploughmarks reflect that the deglaciation occurred – at least to some degree – by iceberg calving.
- The IP₂₅ concentrations and OH-GDGTs reveal rapid changes in sea ice cover and water temperatures during the deglaciation in the time interval *c.* 14.5±0.3 to 11.7±0.3 cal. ka BP representing the coldest period in our study.
- A minimum in sea ice cover prevailed throughout the Early Holocene until around 7 cal. ka BP. Later, sea-ice extent increased and remained high throughout the younger part of the Holocene.
- The low sediment accumulation rate after *c.* 7.6±0.2 cal. ka BP reflects that most of the glaciers in Wijdefjorden, including Longstaffbreen, had retreated onto land by then.
- A clear difference in sediment accumulation rate between core site 1076 (outer) and 1079 (inner) in the late part of the Holocene (L3) indicates that site 1076 (outer) received more sediments from Femmilsjøen, due to its location north of the outlet.
- The increase in sediment accumulation rates after *c.* 0.5 cal. ka BP and the presence of IRD indicate increased activity of the local glaciers in Wijdefjorden. Concurrent stable low water temperatures and increased IP₂₅ concentrations indicate cooler conditions. All this represents the onset of the Little Ice Age in the Wijdefjorden area.

Acknowledgements. – We thank the crew and captain on R/V ‘Helmer Hanssen’, as well as Steinar Iversen, Truls Holm, Alfred Hanssen and André Pedersen for their assistance at sea. We would like to thank Dr Seung-Il Nam (KOPRI) and Dr Mo Hee Kang (KIGAM) for cruise collaboration and scientific discussions. The UiT laboratory engineers Trine M. Dahl, Karina Monsen and Ingvild Hald are thanked for their assistance during the laboratory work. Denise Diekstall and Jens Hefter (AWI) are greatly acknowledged for organic geochemical lab work. We thank Simon Belt for providing the 7-HND standard, Gustav Pallisgaard-Olesen for help with plotting the heat maps, as well as Alix Cage for help with picking foraminifera. Katrine Husum, Jan Sverre Laberg, Emmelie Åström, Wesley R. Farnsworth and Ingrid Leirvik Olsen are acknowledged for constructive data discussions. Anne Hormes and the students of UiT-course GEO-3136/8136 are thanked for their help with testing various inputs into the age-depth model. The laboratory analyses were partly funded by grant no. 17/01132-3 to Lis Allaart from the Svalbard Environmental Protection Fund. Juliane Müller received financial support through a Helmholtz research grant (VH-NG-1101). John Shaw, an anonymous reviewer and Boreas Editor-in-Chief Jan A. Piotrowski are thanked for constructive comments that improved the manuscript.

Author contributions. – LA, MF and AS developed the idea and concept. MF was responsible for the cruise, and selection of coring sites and multibeam survey location. LA and MF participated in the scientific cruise. LA conducted the landform mapping, laboratory work and pre-sampling for the organic geochemical analyses. JM and GM conducted the organic geochemical analyses at AWI. JM helped interpreting the biomarker data and wrote parts of the biomarker section. TAR contributed with import of the geophysical data. LH and SEK contributed with structuring the paper in the early writing phase. LA wrote the main part of the manuscript and created the figures with contributions from all co-authors.

References

- Aagaard, K. 1982: Inflow from the Atlantic Ocean to the Polar Basin. In Rey, L. & Stonehouse, B. (eds.): *The Arctic Ocean: The Hydrographic Environment and the Fate of Pollutants*, 69–81. Palgrave Macmillan, London.
- Aagaard, K., Foldvik, A. & Hillman, S. 1987: The West Spitsbergen Current: disposition and water mass transformation. *Journal of Geophysical Research: Oceans* 92, 3778–3784.
- Adakudlu, M., & 41 others. 2019: Climate in Svalbard 2100. *Norwegian Centre for Climate Services Reports*. The Norwegian Centre for Climate Services (NCCS), <http://bora.uib.no/handle/1956/19136>.
- Allaart, L., Friis, N., Ingólfsson, Ó., Håkansson, L., Noormets, R., Farnsworth, W. R., Mertes, J. & Schomacker, A. 2018: Drumlins in the Nordenskiöldbreen forefield, Svalbard. *GFF* 140, 170–188.
- Andrews, J. T. & Syvitski, J. P. M. 1994: Sediment fluxes along high-latitude glaciated continental margins: Northeastern Canada and Eastern Greenland. In Hay, W. (ed.): *Material Fluxes on the Surface of the Earth*, 99–115. National Academy Press, Washington D.C.
- Andrews, J. T., Milliman, J. D., Jennings, A. E., Rynes, N. & Dwyer, J. 1994: Sediment thickness and Holocene glacial marine sedimentation rates in three East Greenland fjords (ca. 68°N). *The Journal of Geology* 6, 669–683.
- Aradóttir, N., Ingólfsson, Ó., Noormets, R., Benediktsson, Í. Ó., Ben-Yehoshua, D., Håkansson, L. & Schomacker, A. 2019: Glacial geomorphology of Trygghamna, western Svalbard – integrating terrestrial and submarine archives for a better understanding of past glacial dynamics. *Geomorphology* 344, 75–89.
- Baeten, N. J., Forwick, M., Vogt, C. & Vorren, T. O. 2010: Late Weichselian and Holocene sedimentary environments and glacial activity in Billefjorden, Svalbard. *Geological Society, London, Special Publications* 344, 207–223.
- Bartels, M., Titschack, J., Fahl, K., Stein, R. & Hebbeln, D. 2018: Wahlenbergfjord, eastern Svalbard: a glacier-surrounded fjord reflecting regional hydrographic variability during the Holocene? *Boreas* 47, 1003–1021.
- Bartels, M., Titschack, J., Fahl, K., Stein, R., Seidenkrantz, M.-S., Hillaire-Marcel, C. & Hebbeln, D. 2017: Atlantic Water advection vs. glacier dynamics in northern Spitsbergen since early deglaciation. *Climate of the Past* 13, 1717–1749.
- Batchelor, C., Dowdeswell, J. & Hogan, K. 2011: Late Quaternary ice flow and sediment delivery through Hinlopen Trough, Northern Svalbard margin: submarine landforms and depositional fan. *Marine Geology* 284, 13–27.
- Belt, S. T. 2018: Source-specific biomarkers as proxies for Arctic and Antarctic sea ice. *Organic Geochemistry* 125, 277–298.
- Benn, D. & Evans, D. 2010: *Glaciers and Glaciation*. 802 pp. Hodder Arnold Publication, London.
- Beszczynska-Möller, A., Woodgate, R. A., Lee, C., Melling, H. & Karcher, M. 2011: A synthesis of exchanges through the main oceanic gateways to the Arctic Ocean. *Oceanography* 24, 82–99.
- van der Bilt, W. G., Bakke, J., Vasskog, K., D’Andrea, W. J., Bradley, R. S. & Ólafsdóttir, S. 2015: Reconstruction of glacier variability from lake sediments reveals dynamic Holocene climate in Svalbard. *Quaternary Science Reviews* 126, 201–218.
- Bindschadler, R. 2006: Hitting the ice sheets where it hurts. *Science* 311, 1720–1721.

- Blaauw, M. 2010: Methods and code for 'classical' age-modelling of radiocarbon sequences. *Quaternary Geochronology* 5, 512–518.
- Blaauw, M. & Christen, J. A. 2011: Flexible paleoclimate age-depth models using an autoregressive gamma process. *Bayesian Analysis* 6, 457–474.
- Blake, W. 2006: Occurrence of the *Mytilus edulis* complex on Nordaustlandet, Svalbard: radiocarbon ages and climatic implications. *Polar Research* 25, 123–137.
- Błaszczyk, M., Jania, J. A. & Hagen, J. O. 2009: Tidewater glaciers of Svalbard: recent changes and estimates of calving fluxes. *Polish Polar Research* 30, 85–142.
- Blott, S. J. & Pye, K. 2001: GRADISTAT: a grain size distribution and statistics package for the analysis of unconsolidated sediments. *Earth Surface Processes and Landforms* 26, 1237–1248.
- Braun, C. 2019: *Late Weichselian and Holocene glacier dynamics and sedimentary processes in and north of the Wijdefjorden-Austfjorden fjord system, north Spitsbergen*. M.Sc. thesis, UiT the Arctic University of Norway, 111 pp.
- Clark, C. D. 1993: Mega-scale glacial lineations and cross-cutting ice-flow landforms. *Earth Surface Processes and Landforms* 18, 1–29.
- Cook, A. J., Holland, P. R., Meredith, M. P., Murray, T., Luckman, A. & Vaughan, D. G. 2016: Ocean forcing of glacier retreat in the western Antarctic Peninsula. *Science* 353, 283–286.
- Cottier, F. R., Nilsen, F., Skogseth, R., Tverberg, V., Skarøhamar, J. & Svendsen, H. 2010: Arctic fjords: a review of the oceanographic environment and dominant physical processes. *Geological Society, London, Special Publications* 344, 35–50.
- Cuven, S., Francus, P. & Lamoureux, S. 2011: Mid to Late Holocene hydroclimatic and geochemical records from the varved sediments of East Lake, Cape Bounty, Canadian High Arctic. *Quaternary Science Reviews* 30, 2651–2665.
- Dallmann, W. K. 2015: Geoscience atlas of Svalbard. *Norwegian Polar Institute, Report Series No. 148*, 292 pp.
- Davies, S. J., Lamb, H. F. & Roberts, S. J. 2015: Micro-XRF core scanning in palaeolimnology: recent developments. In Croudace, I. W. & Rothwell, R. G. (eds.): *Micro-XRF Studies of Sediment Cores: Applications of a Non-Destructive Tool for the Environmental Sciences*, 189–226. *Developments in Palaeoenvironmental Research* 17. Springer Science+Business Media, Dordrecht.
- Dowdeswell, J. A., Hogan, K., Evans, J., Noormets, R., Ó Cofaigh, C. & Ottesen, D. 2010: Past ice-sheet flow east of Svalbard inferred from streamlined subglacial landforms. *Geology* 38, 163–166.
- Elverhøi, A., Andersen, E. S., Dokken, T., Hebbeln, D., Spielhagen, R., Svendsen, J. I., Sørflaten, M., Rørnes, A., Hald, M. & Forsberg, C. F. 1995b: The growth and decay of the Late Weichselian ice sheet in western Svalbard and adjacent areas based on provenance studies of marine sediments. *Quaternary Research* 44, 303–316.
- Elverhøi, A., Liestøl, O. & Nagy, J. 1980: Glacial erosion, sedimentation and microfauna in the inner part of Kongsfjorden, Spitsbergen. *Norsk Polarinstitutt Skrifter* 172, 33–58.
- Elverhøi, A., Lønne, Ø. & Selander, R. 1983: Glaciomarine sedimentation in a modern fjord environment, Spitsbergen. *Polar Research* 1, 127–150.
- Elverhøi, A., Svendsen, J. I., Solheim, A., Andersen, E. S., Milliman, J., Mangerud, J. & Hooke, R. L. 1995a: Late Quaternary sediment yield from the high Arctic Svalbard area. *The Journal of Geology* 103, 1–17.
- Farnsworth, W. R., Ingólfsson, Ó., Noormets, R., Allaart, L., Alexanderson, H., Henriksen, M. & Schomacker, A. 2017: Dynamic Holocene glacial history of St. Jonsfjorden, Svalbard. *Boreas* 46, 585–603.
- Farnsworth, W. R., Ingólfsson, Ó., Retelle, M., Allaart, L., Håkansson, L. M. & Schomacker, A. 2018: Svalbard glaciers re-advanced during the Pleistocene-Holocene transition. *Boreas* 47, 1022–1032.
- Farnsworth, W. R., Ingólfsson, Ó., Retelle, M. & Schomacker, A. 2016: Over 400 previously undocumented Svalbard surge-type glaciers identified. *Geomorphology* 264, 52–60.
- Fietz, S., Ho, S. L., Hugué, C., Rosell-Melá, A. & Martínez-García, A. 2016: Appraising GDGT-based seawater temperature indices in the Southern Ocean. *Organic Geochemistry* 102, 93–105.
- Flink, A. E., Noormets, R., Fransner, O., Hogan, K. A., Ó'Regan, M. & Jakobsson, M. 2017: Past ice flow in Wahlenbergfjorden and its implications for late Quaternary ice sheet dynamics in northeastern Svalbard. *Quaternary Science Reviews* 163, 162–179.
- Flink, A. E., Noormets, R., Kirchner, N., Benn, D. I., Luckman, A. & Lovell, H. 2015: The evolution of a submarine landform record following recent and multiple surges of Tunabreen glacier, Svalbard. *Quaternary Science Reviews* 108, 37–50.
- Forwick, M. & Vorren, T. O. 2009: Late Weichselian and Holocene sedimentary environments and ice rafting in Isfjorden, Spitsbergen. *Palaeogeography, Palaeoclimatology, Palaeoecology* 280, 258–274.
- Forwick, M. & Vorren, T. O. 2010: Stratigraphy and deglaciation of the Isfjorden area, Spitsbergen. *Norwegian Journal of Geology/Norsk Geologisk Forening* 90, 163–179.
- Forwick, M., Vorren, T. O., Hald, M., Korsun, S., Roh, Y., Vogt, C. & Yoo, K. C. 2010: Spatial and temporal influence of glaciers and rivers on the sedimentary environment in Sassenfjorden and Tempelfjorden, Spitsbergen. *Geological Society, London, Special Publications* 344, 163–193.
- Fransner, O., Noormets, R., Flink, A. & Hogan, K. 2016: Crag-and-tail landforms in outer Rijpfjorden, Nordaustlandet, Svalbard. *Geological Society, London, Memoirs* 46, 57–58.
- Fransner, O., Noormets, R., Flink, A., Hogan, K. A., Ó'Regan, M. & Jakobsson, M. 2017: Glacial landforms and their implications for glacier dynamics in Rijpfjorden and Duvefjorden, northern Nordaustlandet, Svalbard. *Journal of Quaternary Science* 32, 437–455.
- Fredin, O. 2020: *3D plot of grain size data in sedimentology. MATLAB Central File Exchange*. Available at: <https://www.mathworks.com/matlabcentral/fileexchange/33427-3d-plot-of-grain-size-data-in-sedimentology> (accessed 21.01.2020).
- Grobe, H. 1987: A simple method for the determination of ice-rafted debris in sediment cores. *Polarforschung* 57, 123–126.
- Hagen, J. O., Liestøl, O., Roland, E. & Jørgensen, T. 1993: *Glacier Atlas of Svalbard and Jan Mayen*. 167 pp. Norwegian Polar Institute, Oslo.
- Hald, M. & Korsun, S. 1997: Distribution of modern benthic foraminifera from fjords of Svalbard, European Arctic. *Journal of Foraminiferal Research* 27, 101–122.
- Hald, M., Ebbesen, H., Forwick, M., Godtlibsen, F., Khomenko, L., Korsun, S., Olsen, L. R. & Vorren, T. O. 2004: Holocene paleoceanography and glacial history of the West Spitsbergen area, Euro-Arctic margin. *Quaternary Science Reviews* 23, 2075–2088.
- Hansen, T. 2014: *Late Weichselian and Holocene sedimentary processes and glacier dynamics in Woodfjorden, Bockfjorden and Liefdefjorden, North Spitsbergen*. M.Sc. thesis, UiT the Arctic University of Norway, 152 pp.
- Hanssen-Bauer, I., Solas, M. & Steffensen, E. 1990: The climate of Spitsbergen. *DNMI-Rapport* 39, 40 pp.
- Hogan, K. A., Dowdeswell, J. A., Hillenbrand, C. D., Ehrmann, W., Noormets, R. & Wacker, L. 2017: Subglacial sediment pathways and deglacial chronology of the northern Barents Sea Ice Sheet. *Boreas* 46, 750–771.
- Hormes, A., Gjermundsen, E. F. & Rasmussen, T. L. 2013: From mountain top to the deep sea – Deglaciation in 4D of the northwestern Barents Sea ice sheet. *Quaternary Science Reviews* 75, 78–99.
- Howe, J. A., Moreton, S. G., Morri, C. & Morris, P. 2003: Multibeam bathymetry and the depositional environments of Kongsfjorden and Krossfjorden, western Spitsbergen, Svalbard. *Polar Research* 22, 301–316.
- Hughes, A. L. C., Gyllencreutz, R., Lohne, Ø. S., Mangerud, J. & Svendsen, J. I. 2015: The last Eurasian ice sheets—a chronological database and time-slice reconstruction, DATED-1. *Boreas* 45, 1–45.
- Ingólfsson, Ó. & Landvik, J. Y. 2013: The Svalbard-Barents Sea ice-sheet – Historical, current and future perspectives. *Quaternary Science Reviews* 64, 33–60.
- Jakobsson, M. & Anderson, J. 2016: Corrugation ridges in the Pine Island Bay glacier trough, West Antarctica. *Geological Society, London, Memoirs* 46, 265–266.
- Jakobsson, M., Backman, J., Rudels, B., Nycander, J., Frank, M., Mayer, L., Jokar, W., Sangiorgi, F., Ó'Regan, M., Brinkhuis, H., King, J. & Moran, K. 2007: The early Miocene onset of a ventilated circulation regime in the Arctic Ocean. *Nature* 447, 986–990.

- Jakobsson, M., Gyllencreutz, R., Mayer, L. A., Dowdeswell, J. A., Canals, M., Todd, B. J., Dowdeswell, E. K., Hogan, K. A. & Larter, R. D. 2016: Mapping submarine glacial landforms using acoustic methods. *Geological Society, London, Memoirs* 46, 17–40.
- Jakobsson, M., Ingólfsson, Ó., Long, A. J. & Spielhagen, R. F. 2014: The dynamic Arctic. *Quaternary Science Reviews* 92, 1–8.
- Jakobsson, M., Mayer, L. A., Coakley, B., Dowdeswell, J. A., Forbes, S., Fridman, B., Hodnesdal, H., Noormets, R., Pedersen, R. & Rebesco, M. 2012: The international bathymetric chart of the Arctic Ocean (IBCAO) version 3.0. *Geophysical Research Letters* 39, L12609, <https://doi.org/10.1029/2012GL052219>.
- Jernas, P., Kristensen, D. K., Husum, K., Wilson, L. & Koç, N. 2013: Paleoenvironmental changes of the last two millennia on the western and northern Svalbard shelf. *Boreas* 42, 236–255.
- Jiskoot, H., Boyle, P. & Murray, T. 1998: The incidence of glacier surging in Svalbard: evidence from multivariate statistics. *Computers & Geosciences* 24, 387–399.
- Kempf, P., Forwick, M., Laberg, J. S. & Vorren, T. O. 2013: Late Weichselian and Holocene sedimentary palaeoenvironment and glacial activity in the high-arctic van Keulenfjorden, Spitsbergen. *The Holocene* 23, 1607–1618.
- King, E. C., Hindmarsh, R. C. & Stokes, C. 2009: Formation of megascale glacial lineations observed beneath a West Antarctic ice stream. *Nature Geoscience* 2, 585–588.
- Koç, N., Klitgaard-Kristensen, D., Hasle, K., Forsberg, C. F. & Solheim, A. 2002: Late glacial palaeoceanography of Hinlopen Strait, northern Svalbard. *Polar Research* 21, 307–314.
- Kowalewski, W., Rudowski, S. & Zalewski, S. 1990: Seismoacoustic studies within Wijdefjorden, Spitsbergen. *Polish Polar Research* 11, 287–300.
- Landvik, J. Y., Bondevik, S., Elverhøi, A., Fjeldskaar, W., Mangerud, J., Salvigsen, O., Siegert, M. J., Svendsen, J.-I. & Vorren, T. O. 1998: The last glacial maximum of Svalbard and the Barents Sea area: ice sheet extent and configuration. *Quaternary Science Reviews* 17, 43–75.
- Landvik, J. Y., Brook, E. J., Gualtieri, L., Raisbeck, G., Salvigsen, O. & Yiou, F. 2003: Northwest Svalbard during the last glaciation: ice-free areas existed. *Geology* 31, 905–908.
- Landvik, J. Y., Ingólfsson, Ó., Mienert, J., Lehman, S. J., Solheim, A., Elverhøi, A. & Ottesen, D. 2005: Rethinking Late Weichselian ice-sheet dynamics in coastal NW Svalbard. *Boreas* 34, 7–24.
- Laskar, J., Robutel, P., Joutel, F., Gastineau, M., Correia, A. & Levrard, B. 2004: A long-term numerical solution for the insolation quantities of the Earth. *Astronomy & Astrophysics* 428, 261–285.
- Lewis, C., Todd, B., Sonnichsen, G. & King, T. 2016: Iceberg-seabed interaction on northwestern Makkovik Bank, Labrador Shelf, Canada. *Geological Society, London, Memoirs* 46, 279–280.
- Lovell, H., Benn, D. I., Lukas, S., Ottesen, D., Luckman, A., Hardiman, M., Barr, I. D., Boston, C. M. & Sevestre, H. 2018: Multiple Late Holocene surges of a High-Arctic tidewater glacier system in Svalbard. *Quaternary Science Reviews* 201, 162–185.
- Lü, X., Liu, X.-L., Elling, F. J., Yang, H., Xie, S., Song, J., Li, X., Yuan, H., Li, N. & Hinrichs, K. U. 2015: Hydroxylated isoprenoid GDGTs in Chinese coastal seas and their potential as a paleotemperature proxy for mid-to-low latitude marginal seas. *Organic Geochemistry* 89–90, 31–43.
- Luckman, A., Benn, D. I., Cottier, F., Bevan, S., Nilsen, F. & Inall, M. 2015: Calving rates at tidewater glaciers vary strongly with ocean temperature. *Nature Communications* 6, 8566, <https://doi.org/10.1038/ncomms9596>.
- Mangerud, J. & Svendsen, J. I. 1990: Deglaciation chronology inferred from marine sediments in a proglacial lake basin, western Spitsbergen, Svalbard. *Boreas* 19, 249–272.
- Mangerud, J. & Svendsen, J. I. 1992: The last interglacial-glacial period on Spitsbergen, Svalbard. *Quaternary Science Reviews* 11, 633–664.
- Mangerud, J. & Svendsen, J. I. 2018: The Holocene thermal optimum around Svalbard, Arctic North Atlantic; molluscs show early and exceptional warmth. *The Holocene* 28, 65–83.
- Mangerud, J., Boldstad, M., Elgersma, A., Helliksen, D., Landvik, J. Y., Lønne, I., Lycke, A. K., Salvigsen, O., Sandahl, T. & Svendsen, J. I. 1992: The Last Glacial Maximum on Spitsbergen, Svalbard. *Quaternary Research* 38, 1–31.
- Mangerud, J., Bondevik, S., Gulliksen, S., Hufthammer, A. K. & Høisæter, T. 2006: Marine ¹⁴C reservoir ages for 19th century whales and molluscs from the North Atlantic. *Quaternary Science Reviews* 25, 3228–3245.
- McKay, N. P. & Kaufman, D. S. 2014: An extended Arctic proxy temperature database for the past 2,000 years. *Scientific Data* 1, 140026, <https://doi.org/10.1038/sdata.2014.26>.
- Meier, M. F. & Post, A. 1969: What are glacier surges? *Canadian Journal of Earth Sciences* 6, 807–817.
- Miller, G. H., Landvik, J. Y., Lehman, S. J. & Southon, J. R. 2017: Episodic Neoglacial snowline descent and glacier expansion on Svalbard reconstructed from the ¹⁴C ages of ice-entombed plants. *Quaternary Science Reviews* 155, 67–78.
- Müller, J. & Stein, R. 2014: High-resolution record of late glacial and deglacial sea ice changes in Fram Strait corroborates ice-ocean interactions during abrupt climate shifts. *Earth and Planetary Science Letters* 403, 446–455.
- Müller, J., Werner, K., Stein, R., Fahl, K., Moros, M. & Jansen, E. 2012: Holocene cooling culminates in sea ice oscillations in Fram Strait. *Quaternary Science Reviews* 47, 1–14.
- Nilsen, F. 2007: *Jakten på det varme vannet. Svalbardposten* 37, 20–21.
- Nilsen, F., Cottier, F., Skogseth, R. & Mattsson, S. 2008: Fjord-shelf exchanges controlled by ice and brine production: the interannual variation of Atlantic Water in Isfjorden, Svalbard. *Continental Shelf Research* 28, 1838–1853.
- Norwegian Polar Institute 2019: *TopoSvalbard, topographic map over Svalbard*. <https://toposvalbard.npolar.no/> (accessed on 15.07.2019).
- Nuth, C., Kohler, J., König, M., von Deschwanden, A., Hagen, J. O., Käb, A., Moholdt, G. & Petterson, R. 2013: Decadal changes from a multi-temporal glacier inventory of Svalbard. *The Cryosphere* 7, 1603–1621.
- Ó Cofaigh, C. & Dowdeswell, J. A. 2001: Laminated sediments in glacial marine environments: diagnostic criteria for their interpretation. *Quaternary Science Reviews* 20, 1411–1436.
- Ottesen, D. & Dowdeswell, J. 2006: Assemblages of submarine landforms produced by tidewater glaciers in Svalbard. *Journal of Geophysical Research: Earth Surface* 111, F01016, <https://doi.org/10.1029/2005JF000330>.
- Ottesen, D. & Dowdeswell, J. 2009: An inter-ice-stream glaciated margin: submarine landforms and a geomorphic model based on marine-geophysical data from Svalbard. *Geological Society of America Bulletin* 121, 1647–1665.
- Ottesen, D., Dowdeswell, J., Benn, D., Kristensen, L., Christiansen, H. H., Christiansen, O., Hansen, L., Lebesbye, E., Forwick, M. & Vorren, T. 2008: Submarine landforms characteristic of glacier surges in two Spitsbergen fjords. *Quaternary Science Reviews* 27, 1583–1599.
- Ottesen, D., Dowdeswell, J. A., Landvik, J. Y. & Mienert, J. 2007: Dynamics of the Late Weichselian ice sheet on Svalbard inferred from high-resolution sea-floor morphology. *Boreas* 36, 286–306.
- Ottesen, D., Dowdeswell, J. & Rise, L. 2005: Submarine landforms and the reconstruction of fast-flowing ice streams within a large Quaternary ice sheet: the 2500-km-long Norwegian-Svalbard margin (57°–80°N). *Geological Society of America Bulletin* 117, 1033–1050.
- Park, E., Hefter, J., Fischer, G., Iversen, M. H., Ramondenc, S., Nöthig, E. M. & Mollenhauer, G. 2019: Seasonality of archaeal lipid flux and GDGT-based thermometry in sinking particles of high-latitude oceans: Fram Strait (79°N) and Antarctic Polar Front (50°S). *Biogeosciences* 16, 2247–2268.
- Plassen, L., Vorren, T. O. & Forwick, M. 2004: Integrated acoustic and coring investigation of glacial deposits in Spitsbergen fjords. *Polar Research* 23, 89–110.
- R Core Team. 2017: R: A language and environment for statistical computing. R Foundation for Statistical Computing, Vienna, Austria. Retrieved from <https://www.R-project.org/>.
- Rasmussen, T. L., Forwick, M. & Mackensen, A. 2013: Reconstruction of inflow of Atlantic Water to Isfjorden, Svalbard during the Holocene: correlation to climate and seasonality. *Marine Micropaleontology* 99, 18–28.

- Rasmussen, T. L., Thomsen, E., Ślubowska, M. A., Jessen, S., Solheim, A. & Koç, N. 2007: Paleooceanographic evolution of the SW Svalbard margin (76°N) since 20,000¹⁴Cyr BP. *Quaternary Research* 67, 100–114.
- Reimer, P. J., Bard, E., Bayliss, A., Beck, J. W., Blackwell, P. G., Ramsey, C. B., Buck, C. E., Cheng, H., Edwards, L., Friedrich, M., Grootes, P. M., Guilderson, T. P., Hafliðason, H., Hajdas, I., Hatté, C., Heaton, T. J., Hoffmann, D. L., Hogg, A. G., Hughen, K. A., Kaiser, K. F., Kromer, B., Manning, S. W., Niu, M., Reimer, R. W., Richards, D. A., Scott, E. M., Southon, J. R., Staff, R. A., Turney, C. S. & van der Plicht, J. 2013: IntCal13 and Marine13 radiocarbon age calibration curves 0–50,000 years cal BP. *Radiocarbon* 55, 1869–1887.
- Renssen, H., Goosse, H., Fichefet, T., Brovkin, V., Driesschaert, E. & Wolk, F. 2005: Simulating the Holocene climate evolution at northern high latitudes using a coupled atmosphere-sea ice-ocean-vegetation model. *Climate Dynamics* 24, 23–43.
- Rogers, J. C., Yang, L. & Li, L. 2005: The role of Fram Strait winter cyclones on sea ice flux and on Spitsbergen air temperatures. *Geophysical Research Letters* 32, L06709, <https://doi.org/10.1029/2004GL022262>.
- Rothe, T. O., Bakke, J., Støren, E. W. & Bradley, R. S. 2018: Reconstructing Holocene glacier and climate fluctuations from lake sediments in Vårfluesjøen, northern Spitsbergen. *Frontiers in Earth Science* 6, 91, <https://doi.org/10.3389/feart.2018.00091>.
- Rothe, T. O., Bakke, J., Vasskog, K., Gjerde, M., D'Andrea, W. J. & Bradley, R. S. 2015: Arctic Holocene glacier fluctuations reconstructed from lake sediments at Mitrahavøya, Spitsbergen. *Quaternary Science Reviews* 109, 111–125.
- Salvigsen, O. & Høgvard, K. 2006: Glacial history, Holocene shoreline displacement and palaeoclimate based on radiocarbon ages in the area of Bockfjorden, north-western Spitsbergen, Svalbard. *Polar Research* 25, 15–24.
- Salvigsen, O., Forman, S. L. & Miller, G. H. 1992: Thermophilous molluscs on Svalbard during the Holocene and their paleoclimatic implications. *Polar Research* 11, 1–10.
- Screen, J. A. & Simmonds, I. 2010: The central role of diminishing sea ice in recent Arctic temperature amplification. *Nature* 464, 1334–1337.
- Serreze, M. C. & Barry, R. G. 2011: Processes and impacts of Arctic amplification: a research synthesis. *Global and Planetary Change* 77, 85–96.
- Sevestre, H. & Benn, D. I. 2015: Climatic and geometric controls on the global distribution of surge-type glaciers: implications for unifying model of surging. *Journal of Glaciology* 61, 646–662.
- Sharp, M. 1988: Surging glaciers: behaviour and mechanisms. *Progress in Physical Geography* 12, 349–370.
- Skarðhamar, J. & Svendsen, H. 2010: Short-term hydrographic variability in a stratified Arctic Fjord. *Geological Society, London, Special Publications* 344, 51–60.
- Ślubowska, M. A., Koç, N., Rasmussen, T. L. & Klitgaard-Kristensen, D. 2005: Changes in the flow of Atlantic water into the Arctic Ocean since the last deglaciation: evidence from the northern Svalbard continental margin, 80°N. *Paleoceanography* 20, PA 4014, <https://doi.org/10.1029/2005PA001141>.
- Spielhagen, R. F., Werner, K., Sørensen, S. A., Zamelczyk, K., Kandiano, E., Budeus, G., Husum, K., Marchitto, T. M. & Hald, M. 2011: Enhanced modern heat transfer to the Arctic by warm Atlantic water. *Science* 331, 450–453.
- Stokes, C. R. & Clark, C. D. 2002: Are long subglacial bedforms indicative of fast ice flow? *Boreas* 31, 239–249.
- Straneo, F. & Heimbach, P. 2013: North Atlantic warming and the retreat of Greenland's outlet glaciers. *Nature* 504, 36–43.
- Straneo, F., Hamilton, G. S., Sutherland, D. A., Stearns, L. A., Davidson, F., Hammill, M. O., Stenson, G. B. & Rosing-Asvid, A. 2010: Rapid circulation of warm subtropical waters in a major glacial fjord in East Greenland. *Nature Geoscience* 3, 182–186.
- Streuff, K., Ó Cofaigh, C., Noormets, R. & Lloyd, J. 2017: Submarine landforms and glacial marine sedimentary processes in Lomfjorden, East Spitsbergen. *Marine Geology* 390, 51–71.
- Svendsen, J. I. & Mangerud, J. 1997: Holocene glacial and climatic variations on Spitsbergen, Svalbard. *The Holocene* 7, 45–57.
- Svendsen, H., Beszczynska-Möller, A., Hagen, J. O., Lefauconnier, B., Tverberg, V., Gerland, S., Ørbæk, J. B., Bischof, K., Papucci, C., Zajaczkowski, M., Azzolini, R., Bruland, O., Wiencke, C., Winter, J. & Dallmann, W. 2002: The physical environment of Kongsfjorden-Krossfjorden, an Arctic fjord system in Svalbard. *Polar Research* 21, 133–166.
- Svendsen, J. I., Mangerud, J., Elverhøi, A., Solheim, A. & Schüttenhelm, R. T. E. 1992: The Late Weichselian glacial maximum on western Spitsbergen inferred from offshore sediment cores. *Marine Geology* 104, 1–17.
- Syvitski, J. & Praeg, D. 1989: Quaternary sedimentation in the St. Lawrence Estuary and adjoining areas, Eastern Canada: an overview based on high-resolution seismo-stratigraphy. *Géographie physique et Quaternaire* 43, 291–310.
- Syvitski, J., Andrews, J. T. & Dowdeswell, J. A. 1996: Sediment deposition in an iceberg-dominated glacial marine environment, East Greenland: basin fill implications. *Global and Planetary Change* 12, 251–270.
- Tjallingii, R., Röhl, U., Kölling, M. & Bickert, T. 2007: Influence of the water content on X-ray fluorescence core-scanning measurements in soft marine sediments. *Geochemistry, Geophysics, Geosystems* 8, Q02004, <https://doi.org/10.1029/2006GC001393>.
- Vadakkupuliyambatta, S., Bünz, S., Tasianias, A. & Mienert, J. 2016: Iceberg ploughmarks in the SW Barents Sea imaged using high-resolution P-Cable 3D seismic data. *Geological Society, London, Memoirs* 46, 281–282.
- Vorren, T. O., Edvardsen, M., Hald, M. & Thomsen, E. 1983: Deglaciation of the continental shelf off Southern Troms, North Norway. *Norges geologiske undersøkelser* 380, 173–187.
- Werner, A. 1993: Holocene moraine chronology, Spitsbergen, Svalbard: lichenometric evidence for multiple Neoglaciation advances in the Arctic. *The Holocene* 3, 128–137.
- Werner, K., Müller, J., Husum, K., Spielhagen, R. F., Kandiano, E. S. & Polyak, L. 2016: Holocene sea subsurface and surface water masses in the Fram Strait – comparisons of temperature and sea ice reconstructions. *Quaternary Science Reviews* 147, 194–209.
- Woodworth-Lynas, C. M. T., Josenhans, H. W., Barrie, J. V., Lewis, C. F. M. & Parrott, D. R. 1991: The physical process of seabed disturbance during iceberg grounding and scouring. *Continental Shelf Research* 11, 939–961.